

HyperFusion: A Hypernetwork Approach to Multimodal Integration of Tabular and Medical Imaging Data for Predictive Modeling

Daniel Duenias^a, Brennan Nichyporuk^{b,c}, Tal Arbel^{b,c}, Tammy Riklin Raviv^a, ADNI*

^aBen Gurion University of the Negev, blvd 1, Beer Sheva 84105, Israel

^bCentre for Intelligent Machines, McGill University, 3480 University St, Montreal, QC, H3A 0E9, Canada

^cMila - Quebec AI Institute, 6666 Rue Saint-Urbain, Montréal, QC H2S 3H1, Canada

Abstract

The integration of diverse clinical modalities such as medical imaging and the tabular data extracted from patients' Electronic Health Records (EHRs) is a crucial aspect of modern healthcare. Integrative analysis of multiple sources can provide a comprehensive understanding of the clinical condition of a patient, improving diagnosis and treatment decision. Deep Neural Networks (DNNs) consistently demonstrate outstanding performance in a wide range of multimodal tasks in the medical domain. However, the complex endeavor of effectively merging medical imaging with clinical, demographic and genetic information represented as numerical tabular data remains a highly active and ongoing research pursuit.

We present a novel framework based on hypernetworks to fuse clinical imaging and tabular data by conditioning the image processing on the EHR's values and measurements. This approach aims to leverage the complementary information present in these modalities to enhance the accuracy of various medical applications. We demonstrate the strength and generality of our method on two different brain Magnetic Resonance Imaging (MRI) analysis tasks, namely, brain age prediction conditioned by subject's sex and multi-class Alzheimer's Disease (AD) classification conditioned by tabular data. We show that our framework outperforms both single-modality models and state-of-the-art MRI tabular data fusion methods. A link to our code can be found at <https://github.com/daniel4725/HyperFusion>.

Keywords: Deep Learning, Hypernetworks, Tabular-Imaging Data Fusion, Multimodal, Alzheimer Diagnosis, Brain Age Prediction

1. Introduction

In medical decision-making, clinicians rely on comprehensive patient data, including clinical, genetic, demographic, and imaging information,

to gain an in-depth understanding of an individual's condition, thereby improving diagnostic accuracy and treatment outcomes. Deep Neural Networks (DNNs) consistently achieve state-of-the-art results in a broad spectrum of medical tasks. However, they still fall short of matching human experts' abilities to integrate information from medical imaging and non-imaging data. Images are high-dimensional, continuous, and spatial, while patients' Electronic Health Records (EHRs), formatted as numerical, tabular data, typically comprise low-dimensional quantitative attributes with diverse types, scales, and ranges.

*Data used in preparation of this article were obtained from the Alzheimer's Disease Neuroimaging Initiative (ADNI) database (adni.loni.usc.edu). As such, the investigators within the ADNI contributed to the design and implementation of ADNI and/or provided data but did not participate in analysis or writing of this report. A complete listing of ADNI investigators can be found at: http://adni.loni.usc.edu/wp-content/uploads/how_to_apply/ADNI_Acknowledgement_List.pdf

Vision-Language Models (VLMs), such as CLIP (Contrastive Language–Image Pretraining) (Radford et al., 2021), have demonstrated remarkable success in capturing cross-modal relationships between textual concepts and images. These methods rely on contrastive learning, where the model is trained to align representations of images with their closely related textual descriptions while distinguishing unrelated pairs. However, in the medical domain, challenges arise due to the non-uniform distribution of data (Wang et al., 2023). Specifically, there are often no explicit, one-to-one semantic mappings; the same image can be associated with multiple concepts, and a single concept may correspond to different images.

The fusion of imaging and tabular (rather than textual) data presents an additional complication. Although certain measures, such as size or morphology, can be directly correlated with scanned anatomy, many other clinical and demographic attributes, such as medical laboratory results or patient demographics, offer complementary information independent of imaging data. There is no "correct" or semantic match between a patient's chest X-ray and their body temperature; the latter, being a continuous variable, can take any value within a given range. However, when combined, both sources of data can be used to improve the assessment of conditions such as pneumonia (Huang et al., 2020).

To fully exploit both visual and tabular information, we present a conceptually innovative approach that treats clinical measurements and demographic data as priors, influencing the outcomes of an image analysis network. The entire fusion process is analogous to tuning the auditory output of a radio transmitter by manipulating the frequency (selecting stations) and volume. This central concept is implemented through hypernetworks. Originally introduced by (Ha et al., 2016), the hypernetwork framework consists of a primary network assigned to a specific task and a hypernetwork that generates the weights and biases for specific layers of the primary network. The main strength of this meta-learning framework is that, unlike standard deep models, which remain fixed after training, the primary image-processing network is dynamically adjusted based on the input tabular attributes, even at test time.

The key contributions of this work include: (1) the introduction of HyperFusion, a novel hypernetwork-based framework that effectively fuses imaging and tabular data, where tabular information serves as priors influencing the outcomes of an image analysis network. This dynamic fusion process is shown to be particularly powerful, allowing the image-processing network to be adjusted at test time based on varying input attributes. (2) The application of this framework to two challenging brain MRI analysis tasks: brain age prediction conditioned by sex and classification of Alzheimer's disease (AD), Mild Cognitive Impairment (MCI), and Cognitively Normal (CN) subjects using their clinical, demographic, and genetic data. (3) Empirical results demonstrating that HyperFusion outperforms state-of-the-art methods in both tasks, providing new insights into the integration of imaging and tabular data in medical diagnostics.

The rest of this paper is organized as follows. Section 2 reviews the fusion of imaging and tabular data, including the concept of hypernetworks and their applications, along with

relevant studies on brain age prediction and AD classification. Section 3 introduces our hypernetwork framework, detailing the architectures for each task and key implementation aspects. In Section 4, we describe the experimental setup, including datasets, preprocessing, and training/evaluation procedures, followed by the presentation and discussion of the results. Finally, we conclude in Section 5.

2. Related Work

2.1. Fusion methods

The integration of multiple, diverse medical data modalities is an active area of study (Heiliger et al., 2023). While the fusion of multimodal imaging datasets has been explored for over a decade (Menze et al., 2014; Carass et al., 2017; Sui et al., 2023), the merging of imaging and non-imaging data presents additional challenges, and relevant algorithms are relatively recent.

Fusion strategies for combining medical imaging and tabular data can be categorized into three distinct types, as outlined in (Huang et al., 2020): early fusion, where original or extracted features are concatenated at the input level, e.g., (Chierigato et al., 2022); joint fusion (or intermediate fusion), where the feature extraction phase is learned as part of the fusion model; and late fusion, where predictions or pre-trained high level features are combined at the decision level, as in (Pandeya and Lee, 2021; Prabhu et al., 2022).

In this study, we employ the joint fusion approach to facilitate meaningful interaction between modalities. Due to the inherent disparities between tabular and image data, direct integration is not feasible, necessitating some preprocessing. Early fusion proves inadequate for end-to-end processing, leading to the independent processing of image features and hindering the potential for mutual learning between modalities at the intermediate level. Late fusion, on the other hand, occurs solely at the decision level of trained models, failing to foster mutual learning between modalities. In contrast, joint fusion offers the advantages of end-to-end training as well as the potential to condition modality processing based on each other.

A straightforward and intuitive approach to fuse image and tabular data involves using separate networks for each data type - typically a Multi-Layer Perceptron (MLP) for tabular data and a Convolutional Neural Network (CNN) for imaging. While late fusion methods provide predictions based on collective decisions (Prabhu et al., 2022) - joint fusion frameworks embed each modality into a feature vector followed by vector concatenation (Esmaeilzadeh et al., 2018; El-Sappagh et al., 2020; Venugopalan et al., 2021). However, concatenation methods limit the interaction between tabular data and imaging to high-level descriptors, neglecting fusion in CNN layers where crucial spatial image context is preserved.

More advanced joint fusion techniques apply affine transformation to the image features within the intermediate CNN layers, where the shift and scale parameters are generated by a network that processes another data modality. In (Perez et al., 2018), a Feature-wise Linear Modulation (FiLM) was introduced to condition image processing on text, applied to a visual

question-answering task. Building upon FiLM, (Wolf et al., 2022) introduced the Dynamic Affine Feature Map Transform (DAFT) to fuse brain MRIs and tabular data. However, in these techniques, the interaction between different data types is confined to specific stages of the processing pipeline and linear transformations, potentially limiting the network’s ability to fully exploit the advantages of data fusion.

Addressing a different, yet related problem, (Hager et al., 2023) tackles the scenario where tabular data is assumed to be unavailable during the inference phase but can be utilized during training to leverage semantic dependencies within imaging data. The methodology employs contrastive learning to understand imaging-tabular correspondences. However, as highlighted in Section 1, our work observes that the most relevant tabular features are distinctly present in the imaging data. In certain cases, the tabular data encompasses vital attributes that are challenging or nearly impossible to derive from imaging alone, such as specific protein measurements and metabolic indicators. Moreover, it is worth noting that (Hager et al., 2023) relies on extensive datasets for effective contrastive learning utilization, while our work also addresses situations with smaller datasets lacking comprehensive representation. In such instances, explicitly providing information from the tabular data can prove more beneficial than relying on implicit extraction from the image.

Our work incorporates the concept of conditioning image processing on tabular data by employing a hypernetwork framework. In contrast to other methods, our hypernetwork approach is versatile and comprehensive. Specifically, the proposed hypernetwork learns a general transformation (not necessarily linear) to adapt the parameters transferred to the primary network’s layers, regardless of their architecture or position. This flexibility allows for the fusion of imaging with any other modality regardless of the context.

2.2. Hypernetworks

The notion of hypernetworks, where one network (the hypernetwork) generates the weights and biases for another network (the primary network), was introduced in (Ha et al., 2016). We took inspiration from two distinct hypernetwork applications, one of which is the work of (Littwin and Wolf, 2019). This work utilized 2D images input into a hypernetwork for the reconstruction of depicted 3D objects via the primary network. Another inspiring application is found in the denoising framework presented by (Aharon and Ben-Artzi, 2023), where the hypernetwork was trained to generate primary network parameters conditioned by the latent signal-to-noise ratio (SNR) of the input image.

Hypernetworks have also found applications in the medical domain. In (Wydmański et al., 2023), a hypernetwork framework processes tabular data using random feature subsets. In this context, a random binary mask selects a subset of tabular features, simultaneously serving as the input to the hypernetwork responsible for generating parameters for the feature processing network. However, it is important to note that this approach is unimodal, focusing exclusively on tabular data, and lacks integration with imaging data, a key aspect addressed in our work.

To the best of our knowledge, the use of hypernetworks for the fusion of different data modalities in the medical domain is proposed here for the first time. To showcase our approach, we selected two brain MRI analysis challenges that can potentially benefit from the fusion of imaging and tabular data: brain age prediction, a regression problem, and multi-class classification, involving categorization into AD, MCI and CN. More details about these tasks are provided below.

2.3. Brain age prediction

The task of predicting human age based on brain anatomy has garnered significant attention in medical research, driven by the development of AI regression tools and the increasing availability of brain imaging data (Franke and Gaser, 2019; Peng et al., 2021; Lee et al., 2022; Cole and Franke, 2017; Feng et al., 2020; Levakov et al., 2020). Current methods, exclusively based on imaging, demonstrate good prediction accuracy, achieving an average gap of less than three years between the actual chronological age and the predicted brain age of healthy subjects. However, since the primary goal of these studies is the explainability of the neural network, with the aim of providing information on the dynamics of brain aging, relying solely on imaging does not capture other attributes that may influence these processes.

Recognizing the differences in the aging trajectories between men and women (Coffey et al., 1998; Piçarra and Glocker, 2023), we explored whether the incorporation of subject sex information could improve the prediction of brain age. To the best of our knowledge, we are the first to address the task of brain age inference conditioned by the subject’s sex. However, it is essential to note that this exploration is a secondary objective of our study. The primary objective is to showcase and demonstrate our proposed hypernetwork framework, specifically focusing on the fusion of imaging and nonimaging data.

2.4. multi-class AD classification

Early detection of AD from brain MRI is a topic of active research due to its significant implications. The most challenging aspect lies in the classification of individuals with MCI, a transition stage that serves as a potential predictor of the development of AD. Unlike methods designed for binary classification (CN vs AD), such as those presented in (Bäckström et al., 2018; Wang et al., 2018), our focus is on multiclass classification into CN, MCI and AD.

Although many studies addressing this problem rely only on imaging data, as seen in (Wen et al., 2020) and related works, the literature related to neurology suggests the inclusion of clinical and demographic data for enhanced prediction. For example, works such as (Letenneur et al., 1999; Fratiglioni et al., 1991) highlight differences in the hazard ratio of AD between women and men, as well as among individuals with varying levels of educational attainment. The Alzheimer’s Disease Neuroimaging Initiative (ADNI) dataset offers additional tabular data containing essential attributes and biomarkers for AD detection, such as specific protein measurements in the Cerebrospinal Fluid (CSF) and metabolic indicators derived from Positron Emission Tomography (PET) scans.

These additional attributes and their interactions provide relevant information that may not be present in brain MRI scans alone. In recent years, several multimodal fusion methods have been proposed for AD detection (Dolci et al., 2022; Venugopalan et al., 2021; El-Sappagh et al., 2020; Zhou et al., 2019; Liu et al., 2018; Spasov et al., 2018). In this manuscript, we specifically refer to (Wolf et al., 2022; Esmailzadeh et al., 2018; Prabhu et al., 2022), which addressed the fusion of MRIs and tabular data from the ADNI dataset for three-class AD classification.

3. Method

3.1. HyperFusion

The proposed deep learning framework aims to integrate imaging and tabular data to enhance clinical decision making. Figure 1 describes its two main building blocks: a hypernetwork denoted by \mathcal{H}_ϕ and a primary network \mathcal{P}_θ , where ϕ and θ represent their respective parameters. For simplicity, we denote the entire network compound by $\mathcal{F} = \{\mathcal{H}_\phi, \mathcal{P}_\theta\}$.

The input to \mathcal{F} consists of a paired tabular vector of d measurements/values $T \in \mathbb{R}^d$ and a multidimensional image I , specifically a 3D MRI (Figure 1A). Given a tabular vector T , \mathcal{H} produces a data-specific set of network parameters $\theta_{\mathcal{H}} = \mathcal{H}_\phi(T)$, which, combined with internally learned parameters $\theta_{\mathcal{P}}$, forms the entire set of primary network parameters $\theta = \{\theta_{\mathcal{H}}, \theta_{\mathcal{P}}\}$. The output of the primary network $\mathcal{P}_\theta(I)$ represents the desired clinical prediction. In the feedforward pass the input image is fed into the primary network \mathcal{P}_θ (Figure 1C). Simultaneously, the tabular data input is processed by the hypernetwork \mathcal{H}_ϕ (Figure 1B). The hypernetwork block is composed of K sub-networks $\{h_k\}_{k=1, \dots, K}$, each embeds the tabular attributes (see Section 3.1.1), and generates weights and biases $h_k(T) = \theta_{h_k}$ for a corresponding layer in the primary network \mathcal{P}_θ (framed in red). These external parameters of the primary network’s layers depend on T and influence the extracted imaging features accordingly.

During the training phase, the loss backpropagates (yellow arrows) through both the primary and hypernetwork, influencing the learnable parameters $\theta_{\mathcal{P}}$ and ϕ (marked with yellow stars). Specifically, the gradients update the internal primary network layers and only pass through the external ones to update the parameters in the respective hypernetworks. Notably, the external primary network parameters $\theta_{\mathcal{H}}$ are updated indirectly by the hypernetwork (red arrows). This structure allows us to condition the image analysis on the tabular data.

The dependency on tabular data is determined by the ratio between external and internal parameters. To gain insights, let us examine two edge cases. When relying solely on internal network parameters (without a hypernetwork), predictions become indifferent of the tabular information. Conversely, the case where all primary network parameters are external and generated by the hypernetwork, approximates a scenario where separate networks are employed for each combination of tabular attributes. For instance, in brain age prediction, the hypernetwork might generate different parameter sets for men and women. However, while there will be some dependencies thanks to

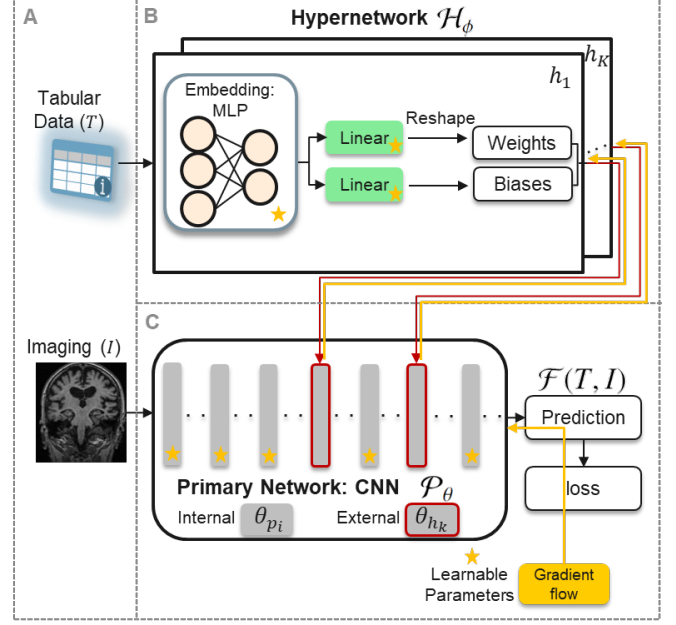


Figure 1: An illustration of the proposed HyperFusion’s Framework. The two main components - hypernetwork and primary network are shown in the upper and the lower part of the figure, respectively. A: The inputs T and I denote tabular and imaging data, respectively. B: The hypernetwork \mathcal{H}_ϕ is composed of K individual networks, $\{h_k\}_{k=1, \dots, K}$, which generate parameters $h_k(T) = \theta_{h_k}$ for specific (external) layers of the primary network \mathcal{P}_θ (red arrows). C: The primary network is composed of internal layers which are updated throughout the backpropagation process (yellow arrows) and external layers (marked in red).

the embedding (Section 3.1.1), having all parameters external would probably necessitate an extended training process with a higher amount of training data. In our configurations, we opted for parameters of low-level primary network layers to be internal, assuming that tabular attributes (e.g., sex) are less likely to be relevant for the extraction of the low level imaging features that eventually contribute to the prediction. This chosen combination of parameter sources allows us to maximize the utilization of available training scans while incorporating the corresponding tabular data for additional gains.

3.1.1. Embedding the tabular data

As depicted in Figure 1B, the proposed hypernetwork generates weights and biases in a two-step process. Initially, the tabular data is input into an embedding network, resulting in a latent vector. Subsequently, this latent vector passes through two distinct linear layers: one for generating weights and another for generating biases. Let $\zeta: \mathbb{R}^d \rightarrow \mathbb{R}^l$ define the embedding function, mapping the tabular data T into a lower dimension space ($l < d$). The desired embedded feature vectors should have a condensed, meaningful representation of the original data, aiming to capture hidden patterns and intricate interactions, while preserving the relevant information. The embedding is a critical step in the fusion process, offering complex associations to the tabular data.

For our tabular embedding network, we opted for an MLP model given that tabular data lacks spatial context. This choice aligns with its favorable performance and suitability for small

datasets, as noted in (Borisov et al., 2022). However, the hypernetwork configuration remains versatile, allowing the integration of any desired embedding architecture.

The proposed framework is end-to-end and the embedding parameters are learned concurrently with the entire network, as illustrated in Figure 1. Moreover, the continuity of the embedding space, where similar samples are mapped closer together, enables interpolation. This capability allows the model to generate meaningful representations for previously unseen samples, enhancing its ability for generalization

3.1.2. Hyperlayer’s position selection

While the proposed hypernetwork concept is general, its adaptation to different applications requires the accommodation to specific architectures of the primary network. Inspired by the layer selection method proposed in (Lutati and Wolf, 2021), we identify ‘good candidates’ for hyperlayers by evaluating the impact of each primary network layer given the untrained, backbone network. The evaluation is carried out by randomly initializing the parameters of the selected layer multiple times ($N = 1000$) while keeping the random parameters of the other network layers fixed. The entropy of the layer-based loss is calculated based on the normalized histogram of the loss values obtained for each random initialization of the layer of interest. Final layer selection from the pool of candidates is conducted empirically as demonstrated in the ablation study in Appendix D.

3.1.3. Weights initialization

A network’s convergence is contingent upon the initial distribution of its parameters. Typically, neural network layer parameters are initialized taking into account their fan-in or fan-out, a practice that stabilizes their convergence, as outlined in (He et al., 2015a; Glorot and Bengio, 2010). In our context, parameter initialization assumes a crucial role, particularly concerning $\theta_{\mathcal{H}}$ generated by the hypernetwork (its output) for the primary network. These parameters are computed as part of the hypernetwork’s feedforward process and cannot be directly initialized to follow a specific distribution. Furthermore, these parameters vary with each different input sample T .

To address this challenge, we employ the technique detailed in (Chang et al., 2019), which performed variance analysis on the hypernetwork output, $\theta_{\mathcal{H}}$. The method aims to initialize the parameters ϕ_k of each hypernetwork k in a way that enables the hypernetwork feedforward process to generate external primary network parameters (θ_{h_k}) fitting a specific distribution. More precisely, the distribution of these parameters should ensure that the output variance in their designated layers within the primary network is closely aligned with the input variance. This initialization contributes to the convergence of the proposed hypernetwork framework.

Formally, let $\phi_k = \{H_k^W, H_k^B\}$ denote the parameters of the fully connected layers of h_k that respectively generate the weights $W_k^j \in \theta_{h_k}$ and the biases $B_k^j \in \theta_{h_k}$ to a hyperlayer j in the primary network. Let d_k and d_j denote the fan-in size of the hypernetwork and the primary network layers, respectively. We also denote by $e(T)$ the embedding (the output of the MLP) of

the pre-processed tabular data and by $\text{Var}(\cdot)$ the variance. To achieve the desired variance, the parameters H_k^M of each hypernetwork k are initialized by sampling from a uniform distribution between $-\sqrt{3\mathcal{V}(H_k^M)}$ and $\sqrt{3\mathcal{V}(H_k^M)}$, where M either stands for the weights W or biases B and $\mathcal{V}(H_k^M)$ is calculated for each set of parameters, as in (Chang et al., 2019) as follows:

$$\mathcal{V}(H_k^W) = \frac{1}{d_j \cdot d_k \cdot \text{Var}(e(T))} \quad (1)$$

$$\mathcal{V}(H_k^B) = \frac{1}{d_k \cdot \text{Var}(e(T))} \quad (2)$$

3.2. Loss functions

As depicted by the yellow arrows in Figure 1 the loss back-propagates throughout the entire network compound affecting both the internal primary network’s parameters and the hypernetwork. Given the flexibility of our framework, the loss function can be adapted to a wide range of applications. It consists of two components the task-specific loss, $\mathcal{L}_{\text{task}}$, and a weight decay regularization term $\mathcal{L}_{\text{regularization}}$ as follows:

$$\mathcal{L}(y, \mathcal{F}(T, I)) = \mathcal{L}_{\text{task}}(y, \mathcal{F}(T, I)) + \mathcal{L}_{\text{regularization}}(\{\phi, \theta_{\mathcal{P}}\}), \quad (3)$$

where, y are the true labels/values. Regularization is applied to ϕ and $\theta_{\mathcal{P}}$ to reduce overfitting. Recall that the external primary network parameters produced by the hypernetwork, i.e., $\theta_{\mathcal{H}}$ do not go through the gradient descent process and therefore are not regularized.

The loss term $\mathcal{L}_{\text{task}}$ in regression tasks is the Mean Square Error (MSE) between the predictions \hat{y} and the ground truth values as follows:

$$\mathcal{L}_{\text{task} = \text{regression}}(y, \hat{y}) = \frac{1}{B} \sum_{i=1}^B (y_i - \hat{y}_i)^2 \quad (4)$$

where B is the batch size and i is the sample index.

For classification tasks with C classes, in order to account for possible class imbalance, we use the Weighted Cross-Entropy (WCE) loss. The weight of each class c is denoted as w^c , and is inversely proportional to the frequency of the class in the training and validation sets. The WCE loss is formulated as follows:

$$\mathcal{L}_{\text{task} = \text{classification}}(\mathbf{P}, \hat{\mathbf{P}}) = - \sum_{i=1}^B \sum_{c=1}^C w^c p_i^c \log(\hat{p}_i^c) \quad (5)$$

where, p_i^c and \hat{p}_i^c denote the ground truth and the predicted probability of class c , respectively, and \mathbf{P} and $\hat{\mathbf{P}}$ are the batched ground truth (one hot) and the predicted distributions.

3.3. Missing values

It is not uncommon to have tabular data with missing values. Handling missing values is a crucial aspect of tabular data pre-processing, as it can significantly impact the quality of modeling and analysis. There exist different strategies to address this challenge. For example, the multi-modal generative approach proposed in (Dolci et al., 2022) which compensates for missing

modalities via a three-module framework. In the first module, each modality is processed independently, the second one imputes the unavailable data using pretrained generators and the last module fuses all features prior to the prediction.

In our study, we impute missing values using an iterative approach. The tabular data is presented as a matrix where each column represents an attribute and each row is a training set sample. In each step, one attribute (column) is selected as the output z , and the remaining columns are considered as inputs X . A regressor is trained on the non missing values of (z, X) , and then employed to predict the missing values of z . This iterative process repeats for each of the columns. As in (Wolf et al., 2022) we add a indicator, such as a NaN flag to indicate imputed values.

While this technique is widely used, it is important to acknowledge potential biases it may introduce. Often, the values of specific attributes are consistently absent from datasets which belong to specific classes. For instance, datasets related to CN subjects typically lack measurements that might pose health risks, requiring invasive procedures or imaging with ionizing radiation. In such cases, the presence of an indicator for missing values could itself be an 'unfair' cue, potentially leading to improved results for the 'wrong reasons'. Additionally, the imputation of attributes with missing values in datasets related to one class might heavily rely on the existing values of another class, potentially compromising their validity. Despite these concerns, we opted for the imputation strategy outlined above to ensure a fair comparison with existing methods that utilize it.

3.4. Ensemble learning

To enhance and stabilize the inference process, we use an ensemble model, denoted as \mathcal{E} , which aggregates the results of M trained models, \mathcal{F}_1 to \mathcal{F}_M . Addressing regression problems, the final prediction is a simple average of the predictions provided by all ensemble's models:

$$\mathcal{E}_{\text{regression}}(T, I) = \frac{1}{M} \sum_{m=1}^M \mathcal{F}_m(T, I). \quad (6)$$

In multi-class classification tasks involving C classes, each model \mathcal{F}_m produces a probability distribution vector over the predicted classes, represented as $\mathbf{p}_m = (p^{c=1}, \dots, p^{c=C})_m$. To obtain the final ensemble prediction, $\mathcal{E}_{\text{classification}}(T, I)$, these models are combined using the weighted average of their probability distributions, as follows:

$$\mathcal{E}_{\text{classification}}(T, I) = \sum_{m=1}^M w_m \mathcal{F}_m(T, I) = \sum_{m=1}^M w_m \mathbf{p}_m. \quad (7)$$

Here w_m defines the weight of the prediction of \mathcal{F}_m in the ensemble. In general, we wish w_m to be higher for models with higher confidence (lower uncertainty). Assuming that the prediction uncertainty positively correlates with its entropy, we set w_m to be inversely proportional to the entropy of network's prediction, as follows:

$$w_m = \frac{J(\mathcal{F}_m(T, I))}{\sum_{i=1}^M J(\mathcal{F}_i(T, I))} = \frac{J(\mathbf{p}_m)}{\sum_{i=1}^M J(\mathbf{p}_i)}, \quad (8)$$

where $J(\cdot)$ is defined by $\frac{1}{H}$ and H is the entropy function. The term $\sum_{i=1}^M J(\mathbf{p}_i)$ serves as a normalization factor.

3.5. Imaging-tabular data fusion applications

To showcase the versatility of the proposed imaging-tabular data fusion framework, we explore two distinct medical imaging applications, each featuring a unique architectural configuration. These applications encompass brain age prediction conditioned by the subject's sex (Section 3.5.1) and multi-class classification of subjects into AD, MCI, and CN groups (Section 3.5.2).

3.5.1. Conditioned brain age prediction using hypernetworks

The proposed hypernetwork framework for conditioned brain age prediction is illustrated in Figure 2. The primary network takes 3D brain MRI scans (T1w) of healthy subjects as input, while the tabular data (single attribute) fed into the hypernetwork consists of 2D one-hot vectors representing the subjects' sex. The hypernetwork compound is trained to address a regression problem using the loss function defined in Equations 3 and 4. The primary network architecture (Figure 2B-C) is a variant of the VGG backbone (Simonyan and Zisserman, 2014), as suggested in (Levakov et al., 2020) for brain age prediction. The parameters of its final four linear layers (framed in red) are external and generated by the hypernetwork. The network output the subjects' brain age ($\in \mathbb{R}$), and the loss function is a weighted sum of the regression loss (MSE) and weight decay regularization, as defined in Equations 3-4. Figure 2C provides a closer look of a convolutional block, comprising two convolutional layers with ReLU activation, batch normalization and downsampling through max-pooling. As illustrated in Figure 2D the hypernetwork comprises four sub-networks (h_1, h_2, h_3, h_4), each corresponds to one of the linear layer in the primary network. Each h_k is composed of a 2-to-1 MLP for the embedding of the one-hot input vectors. The embedding step is crucial, especially when using the orthogonal one-hot representation of the sex attribute (01 or 10). Without embedding, the hypernetwork would generate a distinct set of weights for each sex attribute value. We found that in this case, the most effective integration of the hypernetwork occurred within the linear layers at the final processing stage.

3.5.2. AD classification using hypernetworks

Figure 3 visually presents the hypernetwork framework for multi-class classification of subjects into CN, MCI, and AD groups. The input to the hypernetwork (Figure 3A) is the tabular data which comprise nine clinical and demographic attributes as described in Section 4.3.3. Similar to the brain age prediction's application, the primary network is fed with 3D brain MRI scans (Figure 3B). Yet, for AD classification, the images were cropped to include only the hippocampus and its surrounding tissues as suggested in (Wen et al., 2020). The cropping significantly reduced the input size leading eventually to a reduction in the number of the required network parameters and to better classification results. We note that the hippocampus is the significant component of the limbic lobe being a crucial region for learning and memory. Hippocampal

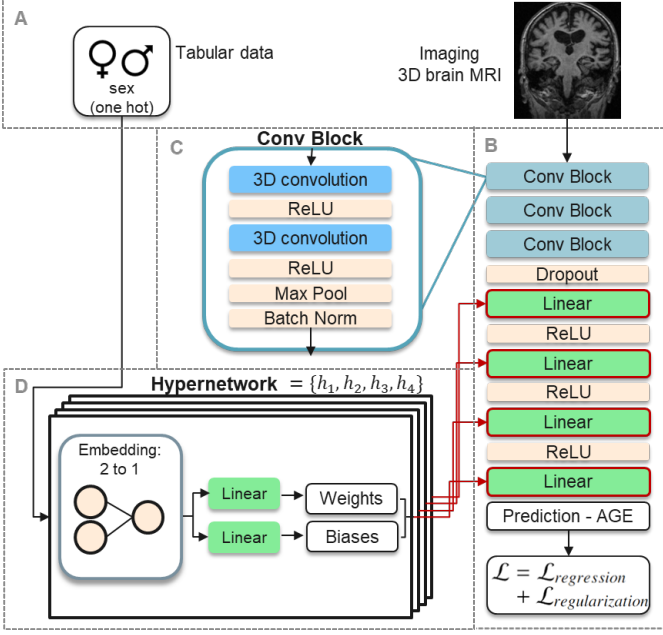


Figure 2: HyperFusion architecture for conditioned brain age prediction. A: The inputs include the subjects’ sex (encoded as a 2D one-hot vector) and the corresponding 3D brain MRIs. B: The primary network backbone is a variant of the VGG architecture (Simonyan and Zisserman, 2014), where the parameters of its final four linear layers (framed in red) are external and generated by the hypernetwork. C: A closer look of a convolutional block. D: The hypernetwork comprises four sub-networks (h_1, h_2, h_3, h_4), each corresponds to one of the linear layer in the primary network.

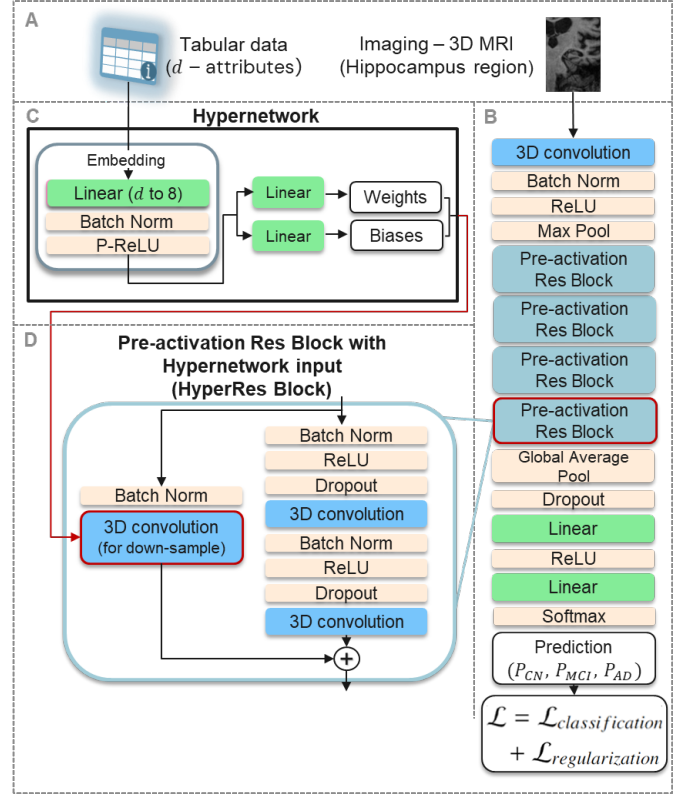


Figure 3: **HyperFusion architecture for the AD classification.** A: The input consists of tabular attributes (d in total) of the subjects along with their brain MRIs. B: The primary network’s is composed of pre-activation ResNet blocks followed by two linear layers. The last ResNet block (framed in red) gets a subset of its parameters from the hypernetwork. The primary network predictions are probability distributions (P_{CN}, P_{MCI}, P_{AD}) produced by the softmax layer. The loss is a weighted sum of the classification loss (weighted CE) and weight decay regularization, as detailed in Equations 3.5. C: The hypernetwork architecture D: A closer look at the pre-activation Res Block. See text for details.

atrophy is a known bio-marker for AD (Rao et al., 2022; Salta et al., 2023). The hypernetwork, illustrated in Figure 3C is composed of a non-linear, single-layer MLP used for embedding, with Parametric ReLU (P-ReLU) (He et al., 2015b). The MLP generates weights and biases for the primary network. The primary network predictions are the probability distributions (P_{CN}, P_{MCI}, P_{AD}) produced by the softmax layer. The loss is a weighted sum of the multi-class classification loss (WCE) and a weight decay regularization term, as detailed in Equations 3.5. The backbone of the primary network, depicted in Figure 3B is based on the pre-activation ResNet blocks followed by two linear layers. The last ResNet block (framed in red), called the HyperRes block, gets a subset of its parameters from the hypernetwork. A closer view of a pre-activation ResNet blocks is presented in Figure 3D. The architecture (based on (He et al., 2016)) is the same for all blocks, yet the illustration specifically refers to the HyperRes block which gets the parameters to one of its convolutional layer (framed in red) from the hypernetwork.

4. Experiments

In this section, we detail the experimental configurations, ablation studies, prediction outcomes, and comparisons for two different brain imaging analysis applications, aiming to showcase the robustness and adaptability of the proposed multi-modal fusion hypernetwork framework. In particular, Section 4.2 delves into the experiments and findings related to

brain age estimation conditioned by the subject’s sex, while Section 4.3 addresses multi-class classification of subjects into CN, MCI, or AD groups. Additional experiments for binary AD classification are presented in Appendix B.

4.1. Experimental details

All the experiments were conducted using a Tesla V100 32 GB GPU with PyTorch. Table 1 presents the experimental details of the AD classification and brain age prediction tasks. All architectural details of the networks are presented in Tables A.5, C.6 in Appendix A.2 and Appendix C.2, respectively.

4.2. Brain age prediction conditioned by sex

While most existing approaches address brain age estimation based on brain MRI data alone, we condition the brain age regression problem on the subject’s sex. We first validate the hypothesis that sex information improves the accuracy of brain age prediction. We then evaluate the efficiency of the hypernetwork framework in fusing imaging and tabular data. This evaluation involves a comparison with the baseline model that exclusively relies on brain MRI data.

Table 1: Experimental details of the AD classification and brain age prediction tasks

Experiment	epochs	batch size	optimizer	weight decay factor	learning rate
Brain age prediction	70	64	ADAM	.05	$1.5 \cdot 10^{-4}$
AD classification	250	32	ADAM	10^{-5}	10^{-4}

4.2.1. The data

The data for this study include 26,691 brain MRI scans of different healthy human subjects from 19 sources. The table in Appendix A.1 presents a comprehensive information on each dataset including the number of subjects as well as their age and sex distributions.

4.2.2. Training and evaluation

We evaluate the hyperfusion and alternative brain-age prediction frameworks using the Mean Absolute Error (MAE) between the chronological and the predicted age. To ensure robustness, we trained multiple models with different random weight initialization to mitigate the potential impact of incidental results. The test results were calculated based on an ensemble of the five best-performing models identified during validation. The ensemble’s output was derived through an average of the model predictions, as detailed in Section 3.4, further enhancing the reliability of our findings.

4.2.3. Preprocessing and partitioning

We applied a preprocessing pipeline to the T1-weighted MRI scans as proposed in (Levakov et al., 2020) - see Appendix A.1 for details. Before being utilized as model inputs, the images were standardized to attain a mean of zero and a standard deviation of one across all non-zero voxels, ensuring data uniformity for effective training. We note that subjects’ sex and age are routinely recorded during the scanning visits. Therefore, we can utilize almost all of the available scans without having to handle issues related to missing values. The tabular data, in this case, consists of a single binary value which is the subject’s sex - male or female. It is represented in our study by a 2D one-hot vector. We partitioned the dataset into training (80%), validation (10%), and test (10%) subsets, preserving consistent age and sex distributions across all the subsets.

4.2.4. Differences in brain aging between males and females

Prior to demonstrating the strength of the proposed hypernetwork integrating imaging and tabular data for the task of brain age prediction conditioned by the subject’s sex we conducted a baseline experiment to support the assumption that the availability of sex information enhances the prediction results. We trained three CNNs, each tailored to a specific dataset: one dedicated to male brain scans, another to female brain scans, and a third to mixed data encompassing both sexes. The mixed dataset, comprising approximately half the volume of the complete dataset, ensured equitable sample representation for each model during training, facilitating a fair comparison. Our evaluations encompassed the entire test set, as well as two subsets—one exclusively featuring male subjects and the other exclusively featuring female subjects.

The MAE scores of obtained by this set of experiments are presented in Figure 4A. The blue, pink and green bars refer

to network training with either male only, female only or mixed data, respectively -maintaining equal-size training sets. The text sets are composed of male only (left), female only (middle) or mixed (right) subsets. The plot strengthens our hypothesis that sex information can facilitate brain age prediction - motivating the proposed hypernetwork framework.

4.2.5. Comparisons and ablation study

Figure 4B presents comparisons of the proposed hyperfusion approach (purple bars) with both image-only (orange bars) and common tabular-imaging concatenation (light blue bars) methods. The comparisons were made for male-only (left bars), female-only (middle bars) and the entire (right bars) test data. For a fair comparison with our hyperfusion model, which provides parameters to all four linear layers in the primary network, the concatenation model combined the sex and image features in each linear layer of the baseline network. Additionally, we performed an ablation study on the embedding of the hypernetwork, specifically comparing our proposed one-hot vector into a single scalar mapping (purple bars) with a mapping into a 2D vector (olive-colored bars). An ablation study assessing the proposed external layer selection can be found in Appendix D.

4.2.6. Results and discussion

The comparisons presented in Figure 4 clearly show that the proposed hyperfusion model outperforms the image-only network for all male-female train-test configurations, as well as the standard concatenation framework. Although beyond the scope of this paper, it is interesting to note that the prediction of female age is much more accurate than the prediction of male age (see the leftmost and middle bars in Figure 4A and B). We assume that this might be due to the greater variability of brain age in males.

4.3. Multi-class AD classification

To further assess the efficiency of our network in fusing imaging and tabular data, we performed a set of experiments on the multi-class AD classification task conditioned by different number and compositions of tabular data attributes. We compared our results to those obtained using either of the data modalities as well as to other existing approaches.

4.3.1. The data

We used four phases of the ADNI databases (ADNI1, ADNI2, ADNI GO, and ADNI3) - selecting a single and complete dataset of each individual (obtained during the first visit). Each of the selected datasets includes a single T-1 MRI scan and the (temporally) corresponding EHR. Statistics of the ADNI data used are presented in Table 2. The information includes the number of samples "N" per label, the mean and standard deviation of age, and the male/female ratio within each diagnostic group. The data used along with the corresponding ADNI’s

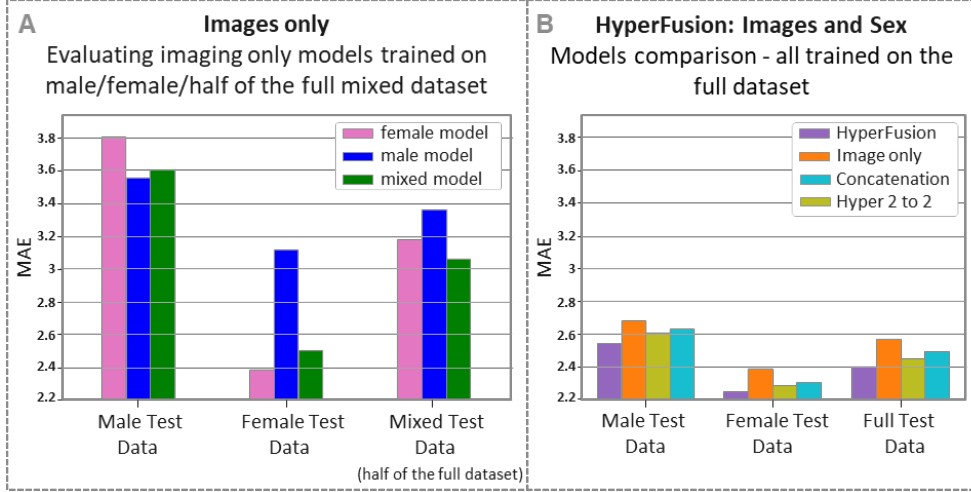


Figure 4: Conditioned brain age prediction results. A) An imaging only experiment. The MAE scores obtained for baseline networks trained on either male only (blue), female only (pink) and mixed (green) equally sized training sets, where the test sets are composed of male only (left), female only (middle) or mixed (right) subsets. B) HyperFusion: A comparison between the baseline model using imaging data alone (orange), concatenation based fusion (light blue), Hyperfusion with different embedding - inputs 2d vector and outputs 2d vector (olive green), and the proposed HyperFusion model (purple) using MAE metric. The inference was performed using either male test data (left), female test data (middle) or the entire (mixed) test dataset (right).

Table 2: Statistics on the CN, MCI and AD sub-populations in our data.

Diagnosis	N (%)	Age - mean (\pm std)	Sex (M:F)
AD	365 (17.2%)	75.1 (\pm 7.8)	(198:167)
CN	740 (34.9%)	72.2 (\pm 6.8)	(309:431)
MCI	1015 (47.9%)	72.8 (\pm 7.6)	(569:446)
Over all	2120 (100%)	73.0 (\pm 7.4)	(1076:1044)

subject identification numbers are available at the Git repository enclosed with this work.

4.3.2. Image preprocessing

The preprocessing pipeline of the MRI scans is similar to the one in Section 4.2.1. As discussed in Section 3.5.2, we cropped the scans into two 3D sub-images of size $64 \times 96 \times 64$ voxels, including either the left or the right hippocampus regions.

4.3.3. Tabular preprocessing

While the subjects’ EHRs contain numerous attributes we chose to use only nine of them. The demographic attributes include age, sex, and education. The CSF biomarkers include $A\beta_{42}$, P-tau181, and T-tau. The third attribute category encompasses composite measures derived from 18F-fluorodeoxyglucose (FDG) and florbetapir (AV45) PET scans. It is important to note that cognitive scores from the EHR were excluded from our study because they were directly used for AD diagnosis. In other words, these scores alone are sufficient for AD classification (Qiu et al., 2018), rendering the entire study meaningless.

Binary (sex) and other discrete attributes were transformed into one-hot vectors. Conversely, attributes with continuous values were centralized and normalized to have zero mean and standard deviation of one. Missing values were handled as described in Section 3.3.

4.3.4. Data partitioning

The dataset is partitioned into five non-overlapping subsets of equal size, ensuring that each subset maintains a similar joint distribution of age, sex, and diagnosis, in accordance with the methodology outlined by (Wen et al., 2020). Among these five subsets, four are allocated for cross-validation, while the fifth is set aside for testing, as depicted in Appendix C.1. The partitioning involves a random shuffling of the data using a predefined random seed, referred to as the split seed. This systematic approach to data splitting enhances the validity and generality of the evaluation process, showcasing the robustness of our model.

4.3.5. Ablation study and comparisons

To evaluate the effectiveness of our proposed HyperFusion approach for image-tabular data fusion, we conducted a comprehensive analysis comparing it with numerous unimodal and multi-modal models. The unimodal models include a baseline MLP designed for tabular data and a pre-activation ResNet optimized for image data processing. Both the baseline MLP and the ResNet are components in our complete hypernetwork compound, as illustrated on the left-hand side of Figure 3C and Figure 3B, respectively.

The imaging-tabular fusion models we compared include various methods. The first one, dubbed ‘concatenation’, involved employing our pre-activation ResNet backbone (presented in Figure 3B) yet, replacing the HyperRes block with a regular pre-activation Res block. The tabular attributes were concatenated with the second-to-last fully connected layer, a technique documented in prior works like (Esmaeilzadeh et al., 2018).

Additionally, we compared our method to the results reported for two contemporary imaging-tabular fusion techniques: the DAFT (Wolf et al., 2022) and the late-fusion approach proposed by (Prabhu et al., 2022). To ensure a fair comparison and high-

light the unique (isolated) contribution of our hypernetwork, we constructed and trained two additional networks. Specifically, we utilized our primary network backbone and training regimen, including our proposed regularized weighted categorical loss function, maintaining the methodologies of FiLM (Perez et al., 2018) (FiLM-like implementation) and DAFT (Wolf et al., 2022) (DAFT-like implementation). We note that our implementation of the FiLM was adapted from (Wolf et al., 2022), since originally the FiLM was designed for text and natural image fusion.

4.3.6. Training and evaluation

We use the Adam optimizer for training, coupled with a regularized WCE loss (Equations 3, 5), as outlined in Sections 3.2 and 3.5.2. The WCE loss accounts for the imbalance between the CN, MCI and AD classes in the training data. However, using standard categorical cross entropy loss while over-sampling the less frequent classes can handle the class imbalance problem as well. The embedding MLP, discussed in detail in Section 3.5.2 and depicted in Figure 3C, underwent pre-training exclusively with the training tabular data to expedite the convergence of the entire network compound.

As mentioned in Section 3.5.2, each subject’s imaging data includes two 3D subimages of the left and right hippocampus. During training, we augment the dataset by randomly selecting either subimage in each feed-forward iteration. For better predictions during validation and testing, we processed each subject’s data twice, once for each brain side, and averaged the soft decisions. Furthermore, we achieved enhanced test results employing an ensemble model, as elaborated in Section 3.4.

To guarantee the robustness of our findings, we adopted an extensive cross-validation strategy encompassing three unique split seeds, each undergoing three rounds of random initialization (versions). In every cross-validation iteration, four models were trained and validated on distinct data folds. For effective result utilization, the four models from a specific version and split seed were aggregated to assess their collective performance on a shared, unseen test set. A visualization for better understanding the training, validation, and testing processes is provided in Figure C.7 in Appendix C.1.

We used various metrics to assess the performance of our framework and compare it with other models. These metrics include balanced accuracy (BA) and precision (PRC), defined as follows:

$$BA = \frac{1}{3} \sum_c \frac{TP_c}{TP_c + FN_c} \quad (9)$$

$$PRC = \frac{1}{3} \sum_c \frac{TP_c}{TP_c + FP_c} \quad (10)$$

Here, $c \in \{CN, MCI, AD\}$, and TP_c , FN_c , FP_c represent the True Positive, False Negative, and False Positive values of class c , respectively. Additionally, we utilized the macro Area Under the ROC Curve (AUC) and macro F1 score. A macro AUC/F1 score is the arithmetic mean of all per-class AUC/F1 scores. These metrics consider the global performance of the models. For class-specific assessment of each model we also used the

True Positive (TP) rate of each class (TP-CN, TP-MCI, TP-AD). Comprehensive confusion matrices are presented in Appendix C.3 (Figure C.8) for a thorough evaluation.

4.3.7. Results and discussion

In this section, we present a comprehensive comparison between all the models discussed in Section 4.3.5 and our hypernetwork model, evaluating both global and class-specific metrics. The results are summarized in Table 3 and Figure 5. In both the bar plot and the table we present the mean and standard deviation over the test data in all random splits and versions. The compared methods that include ‘DAFT-like*’ and ‘FiLM-like*’ are described in Section 4.3.5.

It is noteworthy that all multi-modal methods consistently outperformed unimodal models in terms of global performance metrics and in nearly all class-specific metrics.

Table 3 also presents the scores reported for DAFT (Wolf et al., 2022) and a late fusion method (Prabhu et al., 2022) for certain metrics, along with the results obtained for the methods we implemented as described in Section 4.3.5. For a fair evaluation of the comparison, we note the following differences.

The late fusion method of (Prabhu et al., 2022) used datasets of 3,256 subjects (35.4% CN, 51.1% MCI, 13.5% AD) from the same ADNI phases that we utilized. The tabular data contained an extensive set of 20 attributes, including patient demographics, medical history, vital signs, neurophysiological test results, cognitive function, and other relevant diagnostic information. Some of these attributes were deliberately excluded from our study, as noted in 4.3.3. Notably, the late fusion method obtained higher PRC scores at the expense of weaker BA results due to the inherent trade-off between these two metrics using imbalanced datasets. By applying class weight adjustments to the loss function during training, we were able to achieve better PRC and BA compared to the reported late fusion method results, despite using fewer subjects and a smaller set of tabular attributes (results are shown in Appendix C.4). The reported DAFT method (Wolf et al., 2022) used datasets of 1,341 subjects (40.3% CN, 40.1% MCI, 19.6% AD) from the same ADNI source and a similar set of tabular attributes. To address the difference in data size, we presented the scores obtained using our implementation of a DAFT-like method (Section 4.3.5) as well.

Overall, the scores obtained for both global and class-specific metrics in comparison to other unimodal as well as multi-modal fusion methods demonstrate the superiority of the proposed hypernetwork framework. The p-values, calculated from the Mann-Whitney U tests, assess the statistical significance of the differences between the results.

5. Discussion and Conclusions

We introduced hypernetworks as a solution to the intricate task of integrating tabular and imaging data. Additionally, we illustrated how these networks can condition the analysis of patients’ brain MRIs based on their EHR data. This interaction between imaging and tabular information enhances the understanding of medical data, facilitating a comprehensive diagnostic process.

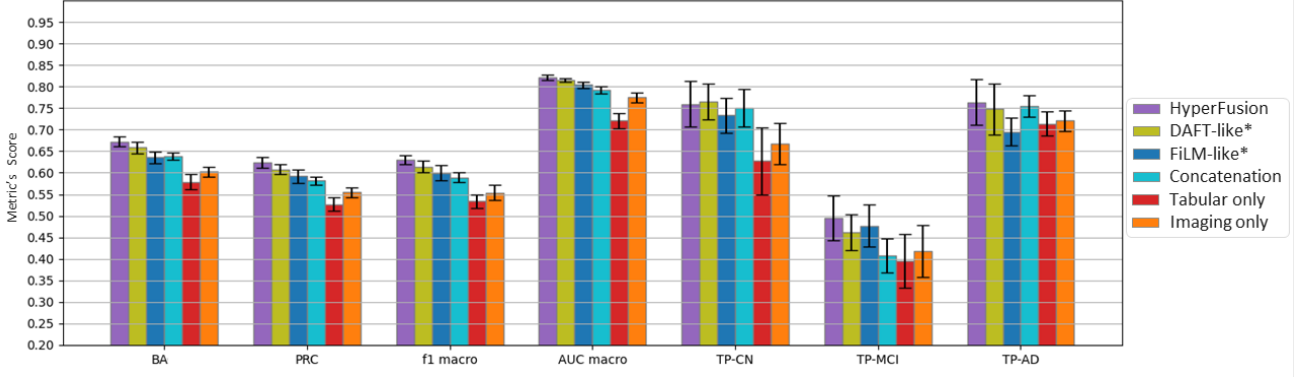


Figure 5: Bar plot presentation of the AD classification results for six competing models and ours using seven different metrics (Section 4.3.6). The compared methods including ‘DAFT-like*’ and ‘FiLM-like*’ are described in Section 4.3.5.

Table 3: AD classification results for the proposed method and other competing models using seven different metrics.

model	BA	PRC	f1 macro	AUC macro	TP-CN	TP-MCI	TP-AD
Imaging only	0.579 ± 0.018 $p < 0.01$	0.527 ± 0.016 $p < 0.01$	0.534 ± 0.016 $p < 0.01$	0.721 ± 0.018 $p < 0.01$	0.627 ± 0.078 $p < 0.01$	0.395 ± 0.063 $p < 0.01$	0.714 ± 0.028 $p < 0.01$
Tabular only	0.602 ± 0.011 $p < 0.01$	0.555 ± 0.011 $p < 0.01$	0.554 ± 0.018 $p < 0.01$	0.775 ± 0.011 $p < 0.01$	0.668 ± 0.048 $p < 0.01$	0.418 ± 0.060 $p < 0.01$	0.721 ± 0.024 $p < 0.01$
Concatenation	0.638 ± 0.008 $p < 0.01$	0.582 ± 0.009 $p < 0.01$	0.589 ± 0.011 $p < 0.01$	0.792 ± 0.008 $p < 0.01$	0.751 ± 0.044 $p = 0.550$	0.408 ± 0.039 $p < 0.01$	0.755 ± 0.025 $p = 0.296$
FiLM-like implementation*	0.635 ± 0.014 $p < 0.01$	0.592 ± 0.016 $p < 0.01$	0.600 ± 0.017 $p < 0.01$	0.804 ± 0.007 $p < 0.01$	0.733 ± 0.040 $p = 0.197$	0.477 ± 0.049 $p = 0.234$	0.696 ± 0.032 $p < 0.01$
DAFT-like implementation*	0.658 ± 0.014 $p < 0.01$	0.608 ± 0.012 $p < 0.01$	0.614 ± 0.014 $p < 0.01$	0.815 ± 0.005 $p < 0.01$	0.765 ± 0.041 $p = 0.717$	0.462 ± 0.042 $p = 0.038$	0.748 ± 0.060 $p = 0.224$
HyperFusion	0.673 ± 0.012	0.624 ± 0.012	0.630 ± 0.011	0.822 ± 0.006	0.759 ± 0.053	0.495 ± 0.052	0.764 ± 0.052
Reported DAFT results (Wolf et al., 2022)	0.622 ± 0.044	-	0.600 ± 0.045	-	0.767 ± 0.080	0.449 ± 0.154	0.651 ± 0.144
Reported late-fusion results (Prabhu et al., 2022)	0.6330	0.6473	0.6240	-	-	-	-

*our adapted implementation as described in Section 4.3.5

The robustness and generality of our method were validated through two distinct clinical applications. The core concepts proposed are adaptable to different network architectures. Furthermore, the straightforward integration of pre-trained networks into our framework promises accelerated convergence and heightened accuracy. Altogether, these aspects position our method as a practical and versatile tool for data fusion.

Our hypernetwork approach surpasses models relying solely on either imaging or tabular data. Unlike many fusion methods, which often use simple concatenation or mixed decisions based on both modalities, including some advanced ones that limit themselves to specific transformations, our method stands out for its increased versatility and degrees of freedom, ensuring superior data utilization in our architectures. Remarkably, when benchmarked against state-of-the-art fusion techniques, our approach not only delivers superior results but also demonstrates their statistical significance.

In this study, we condition the processing of images on the patient’s EHR, adopting an intuitive approach reminiscent of viewing the image through the lens of the patient’s tabular data. An intriguing avenue for future research involves reversing this process: conditioning the EHR analysis on the image. Furthermore, beyond the realms of CNNs and MLPs, exploring the integration of hypernetworks with other architectures opens up

a promising pathway. Such adaptations could pave the way for robust data fusion techniques across a broader spectrum of data modalities.

In summary, this research not only identifies and tackles a crucial deep-learning challenge but also provides a robust solution through hypernetworks. The potential implications of this work extend from improving diagnostics to shaping the broader landscape of personalized medical care. As DNNs in the medical domain continue their rapid evolution, methods like ours, which bridge the gap between diverse data modalities, are poised to play a significant role.

Acknowledgments

Funding: The paper was partially supported by the Ministry of Health (MoH 3-18509. T.R.R.) and the Israel Science Foundation (ISF 2497/19 T.R.R.) Partial funding was provided by the Natural Sciences and Engineering Research Council of Canada (RGPIN-2023-05152), the Canadian Institute for Advanced Research (CIFAR) Artificial Intelligence Chairs program, the Mila - Quebec AI Institute technology transfer program, Calcul Quebec, and the Digital Research Alliance of Canada (alliance.can.ca).

Datasets: Uk-Biobank - This research has been conducted using the UK Biobank Resource (www.ukbiobank.ac.uk).

CORR - Data were provided in part by the Consortium for Reliability and Reproducibility (<http://fcon.1000.projects.nitrc.org/indi/CoRR/html/index.html>)

ADNI - Data collection and sharing for this project was funded by the Alzheimer's Disease Neuroimaging Initiative (ADNI) (National Institutes of Health Grant U01 AG024904) and DOD ADNI (Department of Defense award number W81XWH-12-2-0012). ADNI is funded by the National Institute on Aging, the National Institute of Biomedical Imaging and Bioengineering, and through generous contributions from the following: AbbVie, Alzheimer's Association; Alzheimer's Drug Discovery Foundation; Araclon Biotech; BioClinica, Inc.; Biogen; Bristol-Myers Squibb Company; CereSpir, Inc.; Cogstate; Eisai Inc.; Elan Pharmaceuticals, Inc.; Eli Lilly and Company; EuroImmun; F. Hoffmann-La Roche Ltd and its affiliated company Genentech, Inc.; Fujirebio; GE Healthcare; IXICO Ltd.; Janssen Alzheimer Immunotherapy Research & Development, LLC.; Johnson & Johnson Pharmaceutical Research & Development LLC.; Lumosity; Lundbeck; Merck & Co., Inc.; Meso Scale Diagnostics, LLC.; NeuroRx Research; Neurotrack Technologies; Novartis Pharmaceuticals Corporation; Pfizer Inc.; Piramal Imaging; Servier; Takeda Pharmaceutical Company; and Transition Therapeutics. The Canadian Institutes of Health Research is providing funds to support ADNI clinical sites in Canada. Private sector contributions are facilitated by the Foundation for the National Institutes of Health (www.fnih.org). The grantee organization is the Northern California Institute for Research and Education, and the study is coordinated by the Alzheimer's Therapeutic Research Institute at the University of Southern California. ADNI data are disseminated by the Laboratory for Neuro Imaging at the University of Southern California.

GSP - Data were provided in part by the Brain Genomics Superstruct Project of Harvard University and the Massachusetts General Hospital, (Principal Investigators: Randy Buckner, Joshua Roffman, and Jordan Smoller), with support from the Center for Brain Science Neuroinformatics Research Group, the Athinoula A. Martinos Center for Biomedical Imaging, and the Center for Human Genetic Research. Twenty individual investigators at Harvard and MGH generously contributed data to GSP.

FCP - Data were provided in part by the Functional Connectomes Project (<https://www.nitrc.org/projects/fcon.1000/>).

ABIDE - Primary support for the work by Adriana Di Martino, and Michael P. Milham and his team was provided by the NIMH (K23MH087770), the Leon Levy Foundation, Joseph P. Healy and the Stavros Niarchos Foundation to the Child Mind Institute, NIMH award to MPM (R03MH096321), National Institute of Mental Health (NIMH5R21MH107045), Nathan S. Kline Institute of Psychiatric Research), Phyllis Green and Randolph Cowen to the Child Mind Institute.

PPMI - Data used in the preparation of this article were obtained from the Parkinson's Progression Markers Initiative (PPMI) database (www.ppmi-info.org/data). For up-to-date information on the study, visit www.ppmi-info.org. PPMI—a public-private partnership—is funded by the Michael J. Fox Foundation for Parkinson's Research and funding partners, in-

cluding [list of the full names of all of the PPMI funding partners can be found at www.ppmi-info.org/fundingpartners].

ICBM - Data used in the preparation of this work were obtained from the International Consortium for Brain Mapping (ICBM) database (www.loni.usc.edu/ICBM). The ICBM project (Principal Investigator John Mazziotta, M.D., University of California, Los Angeles) is supported by the National Institute of Biomedical Imaging and BioEngineering. ICBM is the result of efforts of co-investigators from UCLA, Montreal Neurologic Institute, University of Texas at San Antonio, and the Institute of Medicine, Juelich/ Heinrich Heine University-Germany.

AIBL - Data used in the preparation of this article was obtained from the Australian Imaging Bio-markers and Lifestyle flagship study of aging (AIBL) funded by the Commonwealth Scientific and Industrial Research Organization (CSIRO) which was made available at the ADNI database (www.loni.usc.edu/ADNI). The AIBL researchers contributed data but did not participate in analysis or writing of this report. AIBL researchers are listed at www.aibl.csiro.au.

SLIM - Data were provided by the Southwest University Longitudinal Imaging Multimodal (SLIM) Brain Data Repository (http://fcon.1000.projects.nitrc.org/indi/retro/southwestuni_qiu_index.html).

IXI - Data were provided in part by the IXI database (<http://brain-development.org/>).

OASIS - OASIS is made available by Dr. Randy Buckner at the Howard Hughes Medical Institute (HHMI) at Harvard University, the Neuroinformatics Research Group (NRG) at Washington University School of Medicine, and the Biomedical Informatics Research Network (BIRN). Support for the acquisition of this data and for data analysis was provided by NIH grants P50 AG05681, P01 AG03991, P20MH071616, RR14075, RR 16594, U24 RR21382, the Alzheimer's Association, the James S. McDonnell Foundation, the Mental Illness and Neuroscience Discovery Institute, and HHMI.

CNP - This work was supported by the Consortium for Neuropsychiatric Phenomics (NIH Roadmap for Medical Research grants UL1-DE019580, RL1MH083268, RL1MH083269, RL1DA024853, RL1MH083270, RL1LM009833, PL1MH083271, and PL1NS062410).

COBRE - Data were provided by the Center for Biomedical Research Excellence (COBRE) (<http://fcon.1000.projects.nitrc.org/indi/retro/cobre.html>).

CANDI - Data were provided in part by the Child and Adolescent Neuro Development Initiative - Schizophrenia Bulletin 2008 project.

Brainomics - Data were provided in part by the Brainomics project (<http://brainomics.cea.fr/>).

CamCAN - Data collection and sharing for this project was provided by the Cambridge Centre for Ageing and Neuroscience (CamCAN). CamCAN funding was provided by the UK Biotechnology and Biological Sciences Research Council (grant number BB/H008217/1), together with support from the UK Medical Research Council and University of Cambridge, UK.

References

- Aharon, S., Ben-Artzi, G., 2023. Hypernetwork-based adaptive image restoration, in: ICASSP 2023-2023 IEEE International Conference on Acoustics, Speech and Signal Processing (ICASSP), IEEE. pp. 1–5.
- Alexander, L.M., Escalera, J., Ai, L., Andreotti, C., Febre, K., Mangone, A., Vega-Potler, N., Langer, N., Alexander, A., Kovacs, M., et al., 2017. An open resource for transdiagnostic research in pediatric mental health and learning disorders. *Scientific data* 4, 1–26.
- Bäckström, K., Nazari, M., Gu, I.Y.H., Jakola, A.S., 2018. An efficient 3D deep convolutional network for Alzheimer’s disease diagnosis using MR images, in: 2018 IEEE 15th International Symposium on Biomedical Imaging (ISBI 2018), pp. 149–153.
- Biswal, B.B., Mennes, M., Zuo, X.N., Gohel, S., Kelly, C., Smith, S.M., Beckmann, C.F., Adelstein, J.S., Buckner, R.L., Colcombe, S., et al., 2010. Toward discovery science of human brain function. *Proceedings of the national academy of sciences* 107, 4734–4739.
- Borisov, V., Leemann, T., Seßler, K., Haug, J., Pawelczyk, M., Kasneci, G., 2022. Deep neural networks and tabular data: a survey. *IEEE Transactions on Neural Networks and Learning Systems*.
- Buckner, R.L., Roffman, J.L., Smoller, J.W., 2014. Brain Genomics Superstruct Project (GSP).
- Carass, A., Roy, S., Jog, A., et al., 2017. Longitudinal multiple sclerosis lesion segmentation: resource and challenge. *NeuroImage* 148, 77–102.
- Chang, O., Flokas, L., Lipson, H., 2019. Principled weight initialization for hypernetworks, in: International Conference on Learning Representations.
- Chierigato, M., Frangiamore, F., Morassi, M., Baresi, C., Nici, S., Bassetti, C., Bnà, C., Galelli, M., 2022. A hybrid machine learning/deep learning COVID-19 severity predictive model from CT images and clinical data. *Scientific reports* 12, 4329.
- Coffey, C.E., Lucke, J.F., Saxton, J.A., Ratcliff, G., Unitas, L.J., Billig, B., Bryan, R.N., 1998. Sex differences in brain aging: a quantitative magnetic resonance imaging study. *Archives of neurology* 55, 169–179.
- Cole, J.H., Franke, K., 2017. Predicting age using neuroimaging: innovative brain ageing biomarkers. *Trends in neurosciences* 40, 681–690.
- Di Martino, A., Yan, C.G., Li, Q., Denio, E., Castellanos, F.X., Alaerts, K., Anderson, J.S., Assaf, M., Bookheimer, S.Y., Dapretto, M., et al., 2014. The autism brain imaging data exchange: towards a large-scale evaluation of the intrinsic brain architecture in autism. *Molecular psychiatry* 19, 659–667.
- Dolci, G., Rahaman, M.A., Chen, J., Duan, K., Fu, Z., Abrol, A., Menegaz, G., Calhoun, V.D., 2022. A deep generative multimodal imaging genomics framework for alzheimer’s disease prediction, in: 2022 IEEE 22nd International Conference on Bioinformatics and Bioengineering (BIBE), pp. 41–44.
- El-Sappagh, S., Abuhmed, T., Riazul Islam, S., Kwak, K.S., 2020. Multimodal multitask deep learning model for Alzheimer’s disease progression detection based on time series data. *Neurocomputing* 412, 197–215.
- Ellis, K.A., Bush, A.I., Darby, D., De Fazio, D., Foster, J., Hudson, P., Lautenschlager, N.T., Lenzo, N., Martins, R.N., Maruff, P., et al., 2009. The australian imaging, biomarkers and lifestyle (aibl) study of aging: methodology and baseline characteristics of 1112 individuals recruited for a longitudinal study of alzheimer’s disease. *International psychogeriatrics* 21, 672–687.
- Esmaeilzadeh, S., Belivanis, D.I., Pohl, K.M., Adeli, E., 2018. End-to-end Alzheimer’s disease diagnosis and biomarker identification, in: Shi, Y., Suk, H.I., Liu, M. (Eds.), *Machine Learning in Medical Imaging*, Springer International Publishing, Cham. pp. 337–345.
- Feng, X., Lipton, Z.C., Yang, J., Small, S.A., Provenzano, F.A., Initiative, A.D.N., Initiative, F.L.D.N., et al., 2020. Estimating brain age based on a uniform healthy population with deep learning and structural magnetic resonance imaging. *Neurobiology of aging* 91, 15–25.
- Franke, K., Gaser, C., 2019. Ten years of BrainAGE as a neuroimaging biomarker of brain aging: what insights have we gained? *Frontiers in neurology*, 789.
- Fratiglioni, L., Grut, M., Forsell, Y., Viitanen, M., Grafström, M., Holmen, K., Ericsson, K., Bäckman, L., Ahlbom, A., Winblad, B., 1991. Prevalence of Alzheimer’s disease and other dementias in an elderly urban population. *Neurology* 41, 1886–1886.
- Frazier, J.A., Hodge, S.M., Breeze, J.L., Giuliano, A.J., Terry, J.E., Moore, C.M., Kennedy, D.N., Lopez-Larson, M.P., Caviness, V.S., Seidman, L.J., et al., 2008. Diagnostic and sex effects on limbic volumes in early-onset bipolar disorder and schizophrenia. *Schizophrenia bulletin* 34, 37–46.
- Glorot, X., Bengio, Y., 2010. Understanding the difficulty of training deep feedforward neural networks, in: *Proceedings of the thirteenth international conference on artificial intelligence and statistics, JMLR Workshop and Conference Proceedings*. pp. 249–256.
- Gorgolewski, K., Burns, C.D., Madison, C., Clark, D., Halchenko, Y.O., Waskom, M.L., Ghosh, S.S., 2011. Nipype: a flexible, lightweight and extensible neuroimaging data processing framework in python. *Frontiers in neuroinformatics* 5, 13.
- Ha, D., Dai, A.M., Quoc, V.L., 2016. Hypernetworks. *CoRR abs/1609.09106* (2016). arXiv preprint arXiv:1609.09106.

- Hager, P., Menten, M.J., Rueckert, D., 2023. Best of both worlds: Multimodal contrastive learning with tabular and imaging data, in: *Proceedings of the IEEE/CVF Conference on Computer Vision and Pattern Recognition (CVPR)*, pp. 23924–23935.
- He, K., Zhang, X., Ren, S., Sun, J., 2015a. Delving deep into rectifiers: Surpassing human-level performance on imagenet classification, in: *Proceedings of the IEEE international conference on computer vision*, pp. 1026–1034.
- He, K., Zhang, X., Ren, S., Sun, J., 2015b. Delving deep into rectifiers: Surpassing human-level performance on imagenet classification, in: *Proceedings of the IEEE international conference on computer vision*, pp. 1026–1034.
- He, K., Zhang, X., Ren, S., Sun, J., 2016. Identity mappings in deep residual networks, in: Leibe, B., Matas, J., Sebe, N., Welling, M. (Eds.), *Computer Vision – ECCV 2016*, Springer International Publishing, Cham. pp. 630–645.
- Heckemann, R.A., Hartkens, T., Leung, K.K., Zheng, Y., Hill, D.L., Hajnal, J.V., Rueckert, D., 2003. Information extraction from medical images: developing an e-science application based on the globus toolkit, in: *Proceedings of the 2nd UK e-Science All Hands Meeting*.
- Heiliger, L., Sekuboyina, A., Menze, B., Egger, J., Kleesiek, J., 2023. Beyond medical imaging—a review of multimodal deep learning in radiology. *Authorea Preprints*.
- Huang, S.C., Pareek, A., Seyyedi, S., Banerjee, I., Lungren, M.P., 2020. Fusion of medical imaging and electronic health records using deep learning: a systematic review and implementation guidelines. *NPJ digital medicine* 3, 136.
- Iglesias, J.E., Liu, C.Y., Thompson, P.M., Tu, Z., 2011. Robust brain extraction across datasets and comparison with publicly available methods. *IEEE Transactions on Medical Imaging* 30, 1617–1634.
- Jack Jr, C.R., Bernstein, M.A., Fox, N.C., Thompson, P., Alexander, G., Harvey, D., Borowski, B., Britson, P.J., L. Whitwell, J., Ward, C., et al., 2008. The alzheimer’s disease neuroimaging initiative (adni): Mri methods. *Journal of Magnetic Resonance Imaging: An Official Journal of the International Society for Magnetic Resonance in Medicine* 27, 685–691.
- Jenkinson, M., Beckmann, C.F., Behrens, T.E., Woolrich, M.W., Smith, S.M., 2012. Fsl. *NeuroImage* 62, 782–790. 20 YEARS OF fMRI.
- Lee, J., Burkett, B.J., Min, H.K., Senjem, M.L., Lundt, E.S., Botha, H., Graff-Radford, J., Barnard, L.R., Gunter, J.L., Schwarz, C.G., et al., 2022. Deep learning-based brain age prediction in normal aging and dementia. *Nature Aging* 2, 412–424.
- Letenneur, L., Gilleron, V., Commenges, D., Helmer, C., Orgogozo, J.M., Dartigues, J.F., 1999. Are sex and educational level independent predictors of dementia and alzheimer’s disease? incidence data from the paquid project. *Journal of Neurology, Neurosurgery & Psychiatry* 66, 177–183.
- Levakov, G., Rosenthal, G., Shelef, I., Riklin Raviv, T., Avidan, G., 2020. From a deep learning model back to the brain—identifying regional predictors and their relation to aging. *Human Brain Mapping* 41, 3235–3252.
- Littwin, G., Wolf, L., 2019. Deep meta functionals for shape representation, in: *Proceedings of the IEEE/CVF International Conference on Computer Vision*, pp. 1824–1833.
- Liu, M., Zhang, J., Adeli, E., Shen, D., 2018. Joint classification and regression via deep multi-task multi-channel learning for Alzheimer’s disease diagnosis. *IEEE Transactions on Biomedical Engineering* 66, 1195–1206.
- Liu, W., Wei, D., Chen, Q., Yang, W., Meng, J., Wu, G., Bi, T., Zhang, Q., Zuo, X.N., Qiu, J., 2017. Longitudinal test-retest neuroimaging data from healthy young adults in southwest china. *Scientific data* 4, 1–9.
- Lutati, S., Wolf, L., 2021. Hyperhypernetwork for the design of antenna arrays, in: *International Conference on Machine Learning*, PMLR. pp. 7214–7223.
- Marcus, D.S., Fotenos, A.F., Csernansky, J.G., Morris, J.C., Buckner, R.L., 2010. Open access series of imaging studies: longitudinal mri data in nondemented and demented older adults. *Journal of cognitive neuroscience* 22, 2677–2684.
- Marcus, D.S., Wang, T.H., Parker, J., Csernansky, J.G., Morris, J.C., Buckner, R.L., 2007. Open access series of imaging studies (oasis): cross-sectional mri data in young, middle aged, nondemented, and demented older adults. *Journal of cognitive neuroscience* 19, 1498–1507.
- Marek, K., Jennings, D., Lasch, S., Siderowf, A., Tanner, C., Simuni, T., Coffey, C., Kiebertz, K., Flagg, E., Chowdhury, S., Poewe, W., Mollenhauer, B., Klinik, P.E., Sherer, T., Frasier, M., Meunier, C., Rudolph, A., Casaceli, C., Seibyl, J., Mendick, S., Schuff, N., Zhang, Y., Toga, A., Crawford, K., Ansbach, A., De Blasio, P., Piovella, M., Trojanowski, J., Shaw, L., Singleton, A., Hawkins, K., Eberling, J., Brooks, D., Russell, D., Leary, L., Factor, S., Sommerfeld, B., Hogarth, P., Pighetti, E., Williams, K., Standaert, D., Guthrie, S., Hauser, R., Delgado, H., Jankovic, J., Hunter, C., Stern, M., Tran, B., Leverenz, J., Baca, M., Frank, S., Thomas, C.A., Richard, I., Deeley, C., Rees, L., Sprenger, F., Lang, E., Shill, H., Obradov, S., Fernandez, H., Winters, A., Berg, D., Gauss, K., Galasko, D., Fontaine, D., Mari, Z., Gerstenhaber, M., Brooks, D., Malloy, S., Barone, P., Longo, K., Comery, T., Ravina, B., Grachev, I., Gallagher, K., Collins, M., Widnell, K.L., Ostrowizki, S., Fontoura, P., Ho, T., Luthman, J., van der Brug, M., Reith, A.D., Taylor, P., 2011. The parkinson progression marker initiative (ppmi). *Progress in Neurobiology* 95, 629–635. *Biological Markers for Neurodegenerative Diseases*.

- Mayer, A.R., Ruhl, D., Merideth, F., Ling, J., Hanlon, F.M., Bustillo, J., Canive, J., 2013. Functional imaging of the hemodynamic sensory gating response in schizophrenia. *Human brain mapping* 34, 2302–2312.
- Mazziotta, J.C., Toga, A.W., Evans, A., Fox, P., Lancaster, J., 1995. A probabilistic atlas of the human brain: Theory and rationale for its development: The international consortium for brain mapping (icbm). *NeuroImage* 2, 89–101.
- Menze, B.H., Jakab, A., Bauer, S., Kalpathy-Cramer, J., Farahani, K., Kirby, J., Burren, Y., Porz, N., Slotboom, J., Wiest, R., et al., 2014. The multimodal brain tumor image segmentation benchmark (brats). *IEEE transactions on medical imaging* 34, 1993–2004.
- Nooner, K.B., Colcombe, S.J., Tobe, R.H., Mennes, M., Benedict, M.M., Moreno, A.L., Panek, L.J., Brown, S., Zavitz, S.T., Li, Q., et al., 2012. The nki-rockland sample: a model for accelerating the pace of discovery science in psychiatry. *Frontiers in neuroscience* 6, 152.
- Pandeya, Y.R., Lee, J., 2021. Deep learning-based late fusion of multimodal information for emotion classification of music video. *Multimedia Tools and Applications* 80, 2887–2905.
- Peng, H., Gong, W., Beckmann, C.F., Vedaldi, A., Smith, S.M., 2021. Accurate brain age prediction with lightweight deep neural networks. *Medical Image Analysis* 68, 101871.
- Perez, E., Strub, F., de Vries, H., Dumoulin, V., Courville, A., 2018. FiLM: visual reasoning with a general conditioning layer. *Proceedings of the AAAI Conference on Artificial Intelligence* 32.
- Piçarra, C., Glocker, B., 2023. Analysing race and sex bias in brain age prediction, in: *Workshop on Clinical Image-Based Procedures*, Springer. pp. 194–204.
- Pinel, P., Fauchereau, F., Moreno, A., Barbot, A., Lathrop, M., Zelenika, D., Le Bihan, D., Poline, J.B., Bourgeron, T., Dehaene, S., 2012. Genetic variants of foxp2 and kiaa0319/ttrap/them2 locus are associated with altered brain activation in distinct language-related regions. *Journal of Neuroscience* 32, 817–825.
- Poldrack, R.A., Congdon, E., Triplett, W., Gorgolewski, K., Karlsgodt, K., Mumford, J., Sabb, F., Freimer, N., London, E., Cannon, T., et al., 2016. A phenome-wide examination of neural and cognitive function. *Scientific data* 3, 1–12.
- Prabhu, S.S., Berkebile, J.A., Rajagopalan, N., Yao, R., Shi, W., Giuste, F., Zhong, Y., Sun, J., Wang, M.D., 2022. Multimodal deep learning models for Alzheimer’s disease prediction using MRI and EHR, in: *2022 IEEE 22nd International Conference on Bioinformatics and Bioengineering (BIBE)*, IEEE. pp. 168–173.
- Qiu, S., Chang, G.H., Panagia, M., Gopal, D.M., Au, R., Kolachalama, V.B., 2018. Fusion of deep learning models of MRI scans, mini-mental state examination, and logical memory test enhances diagnosis of mild cognitive impairment. *Alzheimer’s and Dementia: Diagnosis, Assessment and Disease Monitoring* 10, 737–749.
- Radford, A., Kim, J.W., Hallacy, C., Ramesh, A., Goh, G., Agarwal, S., Sastry, G., Askell, A., Mishkin, P., Clark, J., et al., 2021. Learning transferable visual models from natural language supervision, in: *International conference on machine learning*, PMLR. pp. 8748–8763.
- Rao, Y., Ganaraja, B., Murlimanju, B., Joy, T., Krishnamurthy, A., Agrawal, A., 2022. Hippocampus and its involvement in Alzheimer’s disease: a review. *3 Biotech* 12.
- Reinhold, J.C., Dewey, B.E., Carass, A., Prince, J.L., 2018. Evaluating the impact of intensity normalization on mr image synthesis. *CoRR abs/1812.04652*. arXiv:1812.04652.
- Salta, E., Lazarov, O., Fitzsimons, P., Tanzi, R., Lucassen, P., Choi, S., 2023. Adult hippocampal neurogenesis in Alzheimer’s disease: A roadmap to clinical relevance. *Cell Stem Cell* 30, 120–136.
- Shafra, M.A., Tyler, L.K., Dixon, M., Taylor, J.R., Rowe, J.B., Cusack, R., Calder, A.J., Marslen-Wilson, W.D., Duncan, J., Dalgleish, T., et al., 2014. The cambridge centre for ageing and neuroscience (cam-can) study protocol: a cross-sectional, lifespan, multidisciplinary examination of healthy cognitive ageing. *BMC neurology* 14, 1–25.
- Simonyan, K., Zisserman, A., 2014. Very deep convolutional networks for large-scale image recognition. *arXiv preprint arXiv:1409.1556*.
- Spasov, S.E., Passamonti, L., Duggento, A., Liò, P., Toschi, N., 2018. A multi-modal convolutional neural network framework for the prediction of Alzheimer’s disease, in: *2018 40th Annual International Conference of the IEEE Engineering in Medicine and Biology Society (EMBC)*, pp. 1271–1274.
- Sudlow, C., Gallacher, J., Allen, N., Beral, V., Burton, P., Danesh, J., Downey, P., Elliott, P., Green, J., Landray, M., et al., 2015. Uk biobank: an open access resource for identifying the causes of a wide range of complex diseases of middle and old age. *PLoS medicine* 12, e1001779.
- Sui, J., Zhi, D., Calhoun, V.D., 2023. Data-driven multimodal fusion: approaches and applications in psychiatric research. *Psychoradiology*, kkad026.
- Tustison, N.J., Avants, B.B., Cook, P.A., Zheng, Y., Egan, A., Yushkevich, P.A., Gee, J.C., 2010. N4itk: Improved n3 bias correction. *IEEE Transactions on Medical Imaging* 29, 1310–1320.
- Venugopalan, J., Tong, L., Hassanzadeh, H.R., Wang, M.D., 2021. Multimodal deep learning models for early detection of Alzheimer’s disease stage. *Scientific reports* 11, 3254.
- Wang, P., Liu, Y., Ko, C.Y., Wells, W.M., Berkowitz, S., Horng, S., Golland, P., 2023. Sample-specific debiasing for better image-text models, in: *Machine Learning for Healthcare Conference*, pp. 788–803.

- Wang, S.H., Phillips, P., Sui, Y., Liu, B., Yang, M., Cheng, H., 2018. Classification of Alzheimer’s disease based on eight-layer convolutional neural network with leaky rectified linear unit and max pooling. *Journal of medical systems* 42, 1–11.
- Wen, J., Thibeu-Sutre, E., Diaz-Melo, M., Samper-González, J., Routier, A., Bottani, S., Dormont, D., Durrleman, S., Burgos, N., Colliot, O., et al., 2020. Convolutional neural networks for classification of Alzheimer’s disease: Overview and reproducible evaluation. *Medical image analysis* 63, 101694.
- Wolf, T.N., Pölsterl, S., Wachinger, C., 2022. DAFT: A universal module to interweave tabular data and 3D images in CNNs. *NeuroImage* 260, 119505.
- Wydmański, W., Bulenok, O., Śmieja, M., 2023. HyperTab: Hypernetwork approach for deep learning on small tabular datasets. *arXiv preprint arXiv:2304.03543*.
- Zhou, T., Thung, K.H., Zhu, X., Shen, D., 2019. Effective feature learning and fusion of multimodality data using stage-wise deep neural network for dementia diagnosis. *Human brain mapping* 40, 1001–1016.
- Zuo, X.N., Anderson, J.S., Bellec, P., Birn, R.M., Biswal, B.B., Blautzik, J., Breitner, J., Buckner, R.L., Calhoun, V.D., Castellanos, F.X., et al., 2014. An open science resource for establishing reliability and reproducibility in functional connectomics. *Scientific data* 1, 1–13.

Appendix

Appendix A. Brain Age Prediction

Appendix A.1. Datasets and Preprocessing

Table A.4 presents the datasets used for the brain age prediction task. The preprocessing pipeline of the T1-weighted MRI scans is identical to the one proposed in (Levakov et al., 2020), using Nipype (Gorgolewski et al., 2011). Initially, RobustFov Jenkinson et al. (2012) was employed to remove the neck and shoulders from each scan. Subsequently, Robex Iglesias et al. (2011) was utilized for brain extraction, followed by expanding the brain mask to encompass the CSF surrounding the brain. The correction for intensity non-uniformity was carried out using N4BiasFieldCorrection Tustison et al. (2010). Further, intensity normalization was implemented using fuzzy c-means and WM-based mean normalization Reinhold et al. (2018). Ultimately, the images were resampled to a resolution of 1.75 mm³ and cropped to a 90x120x99 voxels box centered around the brain mask’s center of mass.

Appendix A.2. Brain Age Prediction Model Architecture

Table A.5 presents the architectural details of the proposed HyperFusion model for brain age prediction presented in Section 3.5.1 of the main paper.

Appendix B. Binary AD classification

We adapted our hypernetwork framework which performs multi-class Alzheimer Disease (AD) classification to address binary classification, thus further demonstrating the strength of our method. The binary classification task is considered less challenging since structural brain differences between AD patients and cognitively normal (CN) subjects are apparent. Nevertheless, there is still a significant gain in integrating both imaging and tabular data using the proposed hypernetwork framework on our sorted ADNI dataset, as is demonstrated in Figure B.6. To further demonstrate the advantage of the proposed hypernetwork framework we fused the soft classification results of both the tabular-only and the imaging-only and present the resulting late-fusion predictions (orange bars) in the figure. While the late-fusion results are better than those obtained by the tabular-only for all metrics and imaging-only for most metrics they are inferior with respect to the hypernetwork performances.

Appendix C. Multiclass AD classification

Appendix C.1. Data splitting, model training and evaluation

Figure C.7 depicts the partition of the ADNI data as well as the evaluation method for the cross validation experiments of the AD classification.

Appendix C.2. AD Classification Model Architecture

Table C.6 presents the architectural details of the proposed HyperFusion model for AD classification presented in Section 3.5.2 of the main paper.

Appendix C.3. AD Classification Confusion Matrices

Figure C.8 presents the confusion matrices obtained by the proposed the hyperfusion model for the AD in comparison to other methods. The confusion matrices provide statistics on the the accurate and inaccurate classification rates of each class.

Appendix C.4. Class Weights for the AD Classification Task

As mentioned in the main manuscript, we trained the hyperfusion framework for multi-class AD classification with weighted categorical cross entropy (WCE) loss, where the weights of the classes (CN, MCI, AD) are approximately inverse-proportional to their frequency. To assess our choice, we performed an ablation study comparing the proposed approach with a prevalent alternative to address data imbalance, an oversampling of the less frequent classes using standard CE loss. The results are presented in Table C.7 showing the advantage of using the WCE loss.

Table A.4: List of all datasets used for the brain age prediction task. For each dataset, the number of available subjects (N), the sex distribution, and the mean and std of the age distribution are provided.

Study/database	N	Age - mean (\pm std)	Sex (M:F)
UK Biobank (Sudlow et al., 2015)	17,088	63.1 (\pm 7.5)	8,118:8,970
Consortium for Reliability and Reproducibility, CoRR (Zuo et al., 2014)	1,350	26.1 (\pm 15.9)	661:689
Alzheimer’s Disease Neuroimaging Initiative, ADNI (Jack Jr et al., 2008)	659	72.9 (\pm 6.0)	432:227
Brain Genomics Superstruct Project, GSP (Buckner et al., 2014)	1,099	21.5 (\pm 2.9)	469:630
Functional Connectomes Project, FCP (Biswal et al., 2010)	922	28.2 (\pm 13.9)	393:529
Autism Brain Imaging Data Exchange, ABIDE (Di Martino et al., 2014)	506	16.9 (\pm 7.7)	411:95
Parkinson’s Progression Markers Initiative, PPMI (Marek et al., 2011)	172	60.3 (\pm 11.0)	105:67
International Consortium for Brain Mapping, ICBM (Mazziotta et al., 1995)	592	30.9 (\pm 12.5)	319:273
Australian Imaging, Biomarkers and Lifestyle, AIBL (Ellis et al., 2009)	604	73.0 (\pm 6.6)	268:335
Southwest University Longitudinal Imaging Multimodal, SLIM (Liu et al., 2017)	571	20.1 (\pm 1.3)	251:320
Information extraction from Images, IXI (Heckemann et al., 2003)	562	48.2 (\pm 16.5)	251:311
Open Access Series of Imaging Studies, OASIS (Marcus et al., 2007, 2010)	401	51.7 (\pm 24.9)	144:257
Consortium for Neuropsychiatric Phenomics, CNP (Poldrack et al., 2016)	124	31.5 (\pm 8.8)	65:59
Center for Biomedical Research Excellence, COBRE (Mayer et al., 2013)	74	35.8 (\pm 11.6)	51:23
Child and Adolescent NeuroDevelopment Initiative, CANDI (Frazier et al., 2008)	29	10.0 (\pm 2.9)	17:12
Brainomics (Pinel et al., 2012)	68	25.4 (\pm 7.1)	31:37
Cambridge Centre for Ageing and Neuroscience, CamCAN (Shafto et al., 2014)	652	54.3 (\pm 18.6)	322:330
Child Mind Institute - Healthy Brain Network, HBN (Alexander et al., 2017)	304	10.0 (\pm 3.7)	164:140
Nathan Kline Institute-Rockland Sample, NKI (Nooner et al., 2012)	914	37.1 (\pm 21.7)	359:555
Overall	26,691	53.7 (\pm 19.5)	12,831:13,859

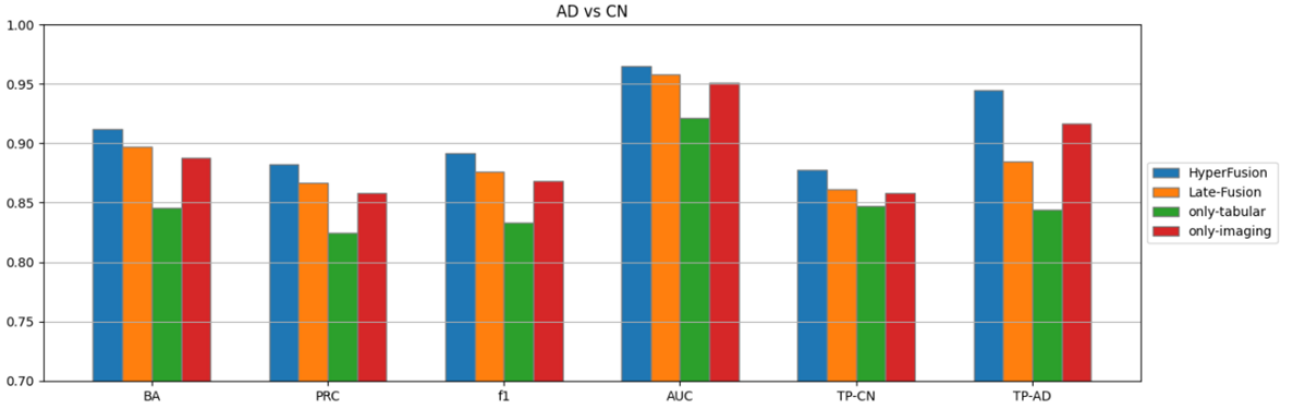


Figure B.6: Binary classification experiments comparing imaging/tabular data single modality and Hyperfusion.

Table A.5: Architecture of the brain age prediction model

Brain Age Prediction Model Architecture			
Index	Name	Type	Params
0	conv1_a	Conv3d	448
1	conv1_b	Conv3d	6.9 K
2	batchnorm1	BatchNorm3d	32
3	conv2_a	Conv3d	13.9 K
4	conv2_b	Conv3d	27.7 K
5	batchnorm2	BatchNorm3d	64
6	conv3_a	Conv3d	55.4 K
7	conv3_b	Conv3d	110 K
8	batchnorm3	BatchNorm3d	128
9	dropout1	Dropout3d	0
10	linear1	HyperLinear	1.3 M
11	linear2	HyperLinear	1.1 K
12	linear3	HyperLinear	4.2 K
13	final_layer	HyperLinear	133
Trainable params			1.5 M
Total params			1.5 M
Total estimated model params size (MB)			5.929

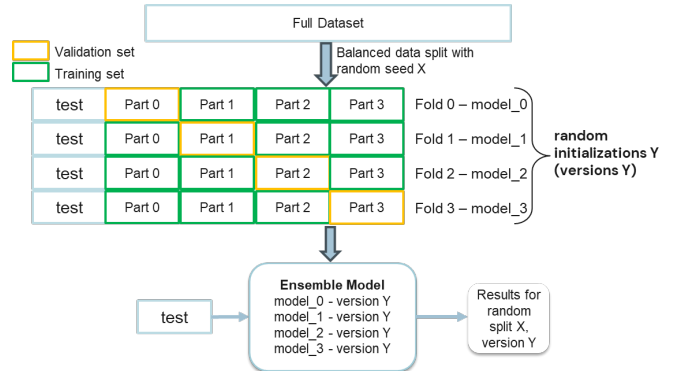


Figure C.7: A schematic illustration of the data splitting and model training and evaluation for multiclass AD classification: each round is based on a different random initialization of a model. The entire process is performed using three random seeds with three versions for each, i.e., nine cross-validation experiments all together.

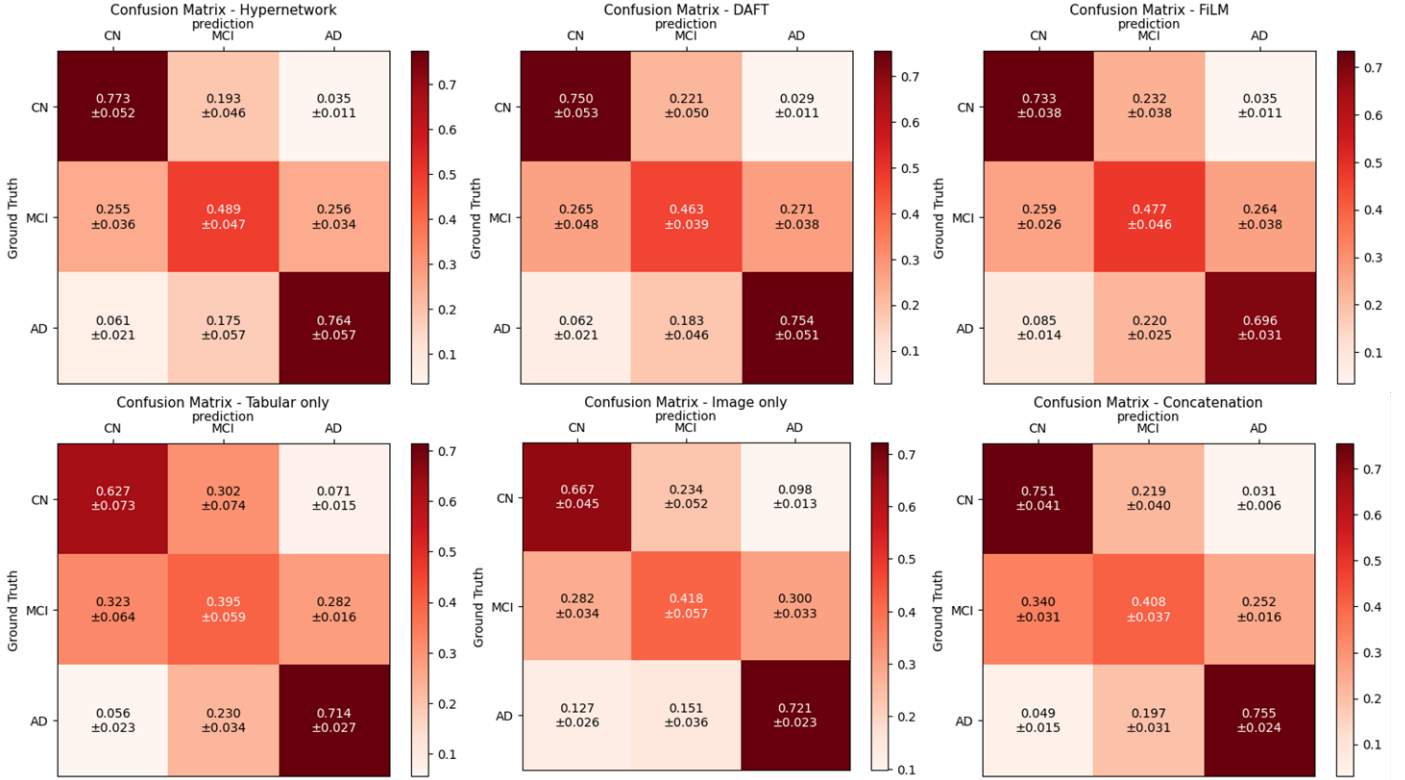


Figure C.8: Confusion matrices for the AD classification task. Each matrix represents the predicted results versus the ground truth, with row-normalization for easier interpretation. Each cell in a matrix contains the mean and standard deviation values calculated over all conducted experiments.

Appendix D. Selection of hyperlayers

As detailed in Section Appendix D in the main paper, there is one hypernetwork embedding for each hyperlayer. The selection of hyperlayer candidates is based on the heuristic suggested in Lutati and Wolf (2021). Specifically, we tested how random weight initializations of a specific layer (while keeping all other weights fixed) influences the loss of the overall network. Calculating the entropy of the loss values we evaluate the impact of that layer. After identifying potential candidate layers, fine-tune selection is conducted empirically.

Appendix D.1. Hyperlayers for Brain Age Prediction Network

Figure D.9.A presents a bar plot showing the loss entropy for each layer in the primary network. The final combination of hyperlayers is chosen based on an ablation study applied to the selected candidates. Figure D.9.B presents a bar plot showing the prediction results (using the validation set) for each combination tested. Based on this experiment four linear layers in the primary network were set as hyperlayers since this combination yielded the lowest Mean Absolute Error (MAE) for brain age prediction.

Appendix D.2. Hyperlayers for AD classification Network

Figure D.10 depicts the entropy of layer-based loss values for each layer in the primary network for AD classification. Figure D.11 presents a bar plot depicting the results of the ablation study conducted for the final determination of the hyperlayers. Both figures visually demonstrate the correlation between the

Table C.6: Architecture of the AD classification model

AD Classification Model Parameters			
Index	Name	Type	Params
0	conv_bn_relu	Sequential	480
1	max_pool3d_1	MaxPool3d	0
2	block1	PreactivResBlock_bn	42.2 K
3	block2	PreactivResBlock_bn	168 K
4	block3	PreactivResBlock_bn	672 K
5	block4	HyperPreactivResBlock	3.0 M
6	adaptive_avg_pool3d	AdaptiveAvgPool3d	0
7	linear_drop1	Dropout	0
8	fc1	LinearLayer	16.4 K
9	linear_drop2	Dropout	0
10	fc2	LinearLayer	195
11	relu	ReLU	0
Trainable params			3.9 M
Total params			3.9 M
Total estimated model params size (MB)			15.415

Table C.7: Hyperfusion performances using WCE/CE loss with/without upsampling

model	BA	PRC	f1 macro	AUC macro	TP-CN	TP-MCI	TP-AD
WCE loss	.673	.624	.630	.822	.759	.495	.764
CE w upsample	.643	.597	.601	.806	.687	.488	.755
CE w/o upsample	.628	.595	.599	.782	.668	.521	.695

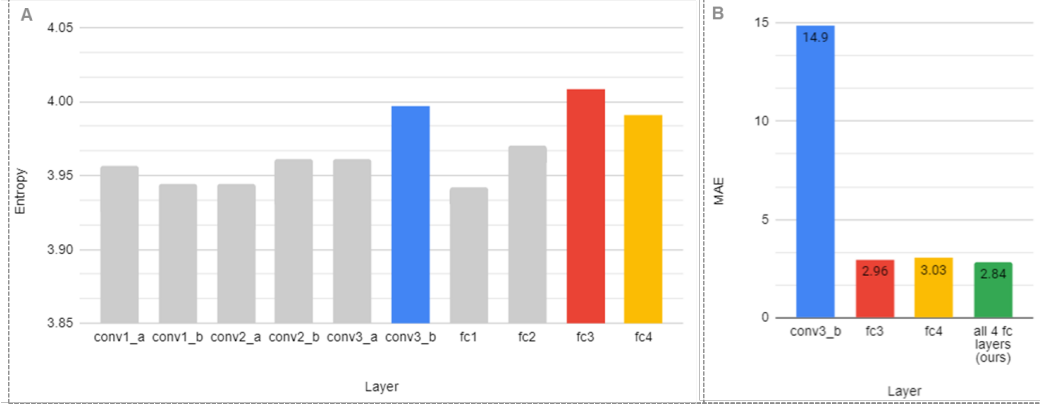


Figure D.9: A. A bar plot representing the entropy of the loss values obtained for random initializations of each primary network layer. $\text{conv } j$ denotes a convolutional layer within the block (conv1 or 2), and $\text{fc } i$ denotes the i th fully connected layer. B. A bar plot depicting the ablation study conducted for the selection of hyperlayer combination. Specifically, the MAE for each selection is presented. Both plots refer to brain age prediction.

Table C.8: AD classification results for the proposed HyperFusion and the late-fusion method. The first row presents the scores obtained our model using different class weight configurations in the weighted cross entropy loss function. The second row presents reported results of the late-fusion method of (Prabhu et al., 2022). The comparison is based on three metrics detailed in main manuscript.

model	BA	PRC	f1 macro
HyperFusion - different class weights	0.6539	0.6563	0.6433
Reported late-fusion results (Prabhu et al., 2022)	0.6330	0.6473	0.6240

loss-based entropy of the convolutional layers, their positions within the network, and the resulting performance. Indeed, the linear layers have higher entropy, yet the final prediction results based on the validation set are inferior when these layers were set to be hyperlayers. In contrast, setting the down-sample convolutional layer in the last Res-block as hyperlayer yielded the best results in all metrics tested (brown bars). This layer was therefore selected.

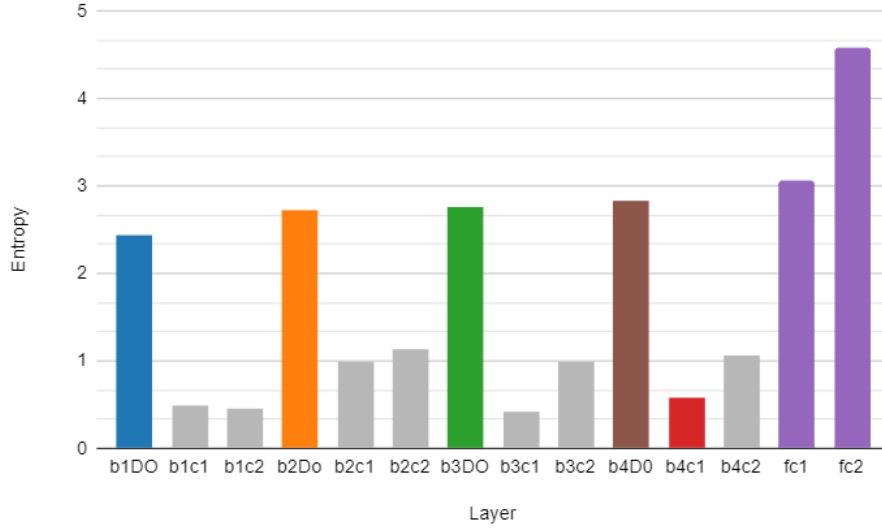


Figure D.10: A bar plot representing the entropy of the loss values obtained for random initialization of each primary network layer for AD classification. b_i denotes the i -th Res-block, and c_j denotes the convolutional layer within the block (conv1 or 2), and fc_i denotes the i th fully connected layer. Gray bars represent layers that have not been empirically tested.

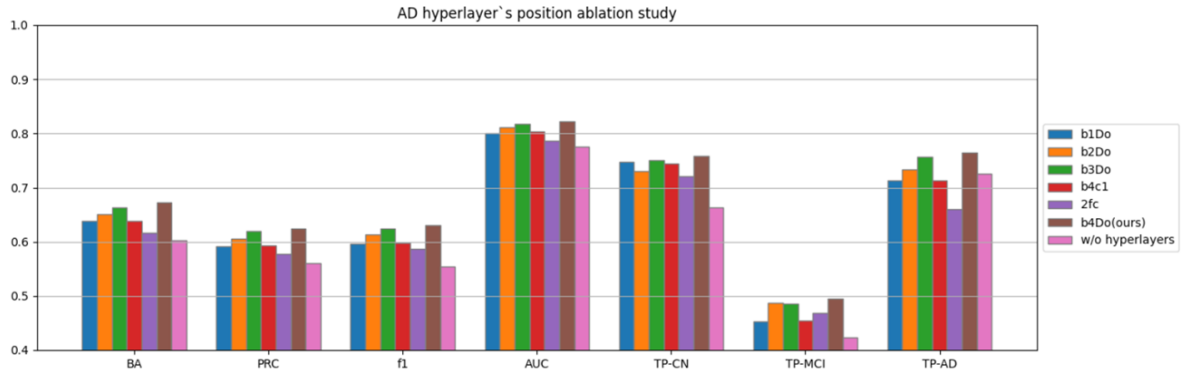


Figure D.11: A bar plot depicting the results of the ablation study conducted for the determination of the hyperlayers for AD classification. BA stands for Balance Accuracy; Prc for percision; AUC stands for the Area Under the ROC Curve (AUC) and f1 stands for the F1 score. $TP-C$ represent the True Positive values of class C , where $C \in \{CN, MCI, AD\}$. The bar colors follow the legend and correspond to these shown in Figure D.10. Legend: DO refers to the downsample convolution inside the block. Other symbols as in Figure D.10.